Check for updates

Recent progresses in the synthesis of MnO2 nanowire and its application in environmental catalysis

Huikang Song,[†][a] Leilei Xu, [ID] [†][*a] Mindong Chen,[*a] Yan Cui,[a] Cai-e Wu,[b] Jian Qiu,[c] Liang Xu,[c] Ge Cheng[a] and Xun Hu [ID] [d]

Nanostructured MnO2 with various morphologies exhibits excellent performance in environmental catalysis owing to its large specific surface area, low density, and adjustable chemical properties. The one-dimensional MnO2 nanowire has been proved to be the dominant morphology among various nanostructures, such as nanorods, nanofibers, nanoflowers, *etc*. The syntheses and applications of MnO2-based nanowires also have become a research hotspot in environmental catalytic materials over the last two decades. With the continuous deepening of the research, the control of morphology and crystal facet exposure in the synthesis of MnO2 nanowire materials have gradually matured, and the catalytic performance also has been greatly improved. Differences in the crystalline phase structure, preferably exposed crystal facets, and even the length of the MnO2 nanowires will evidently affect the final catalytic performances. Besides, the modifications by doping or loading will also significantly affect their catalytic performances. This review carefully summarizes the synthesis strategies of MnO2 nanowires developed in recent years as well as the influences of the phase structure, crystal facet, morphology, dopant, and loading amount on the catalytic performance. Besides, the cutting-edge applications of MnO2 nanowires in the field of environmental catalysis, such as CO oxidation, the removal of VOCs, denitrification, *etc*., have been also summarized. The application of MnO2 nanowire in environmental catalysis is still in the early exploratory stage. The gigantic gap between theoretical investigation and industrial application is still a great challenge. Compared with noble metal based traditional environmental catalytic materials, the lower cost of MnO2 has injected new momentum and promising potential into this research field.

1. Introduction

The worldwide emissions of atmospheric pollutants, such as CO and volatile organic compounds (VOCs), have greatly increased year by year with the rapid development of the global economy.[1,2] For example, CO is generally regarded as a flammable, explosive, and toxic air pollutant, which is extremely harmful to human health and the living environment.[3–6] Besides, it is also a weak direct greenhouse gas and has an

important indirect effect on global warming.[7–10] Generally, CO is mainly derived from the incomplete combustion of fuels.[11,12] As for the VOCs, they commonly include formaldehyde, benzene, toluene, xylene, *etc*.[2] They can enter into the human body through breathing and skin permeation, causing discomfort to the body and even inducing cancer. Besides, VOCs are also considered as important precursors of high concentrations of $PM_{2.5}$ and O_3 in the atmosphere. Therefore, it is greatly necessary to develop efficient technologies to control the emissions of CO, VOCs, and other atmospheric pollutants. The current technologies mainly include adsorption, separation, biodegradation, catalytic combustion, plasma coordinated catalysis, photocatalysis, *etc*. Among these strategies, the catalytic oxidation or combustion has attracted increasing attention due to the advantages of high purification efficiency, low reaction temperature, and low cost. Therefore, designing and developing the catalysts with advanced performances are the key solutions to the catalytic oxidation of these air pollutants.

Noble metals (Au,[13,14] Pt,[15–17] Pd,[18] and Rh[19]) supported on particular metal oxides (CeO_2, $Ce_xZr_{1−x}O_2$ and Fe_2O_3) with excellent oxygen storage capacities usually perform high

[a]*Collaborative Innovation Centre of the Atmospheric Environment and Equipment Technology, School of Environmental Science and Engineering, Nanjing University of Information Science & Technology, Jiangsu Key Laboratory of Atmospheric Environment Monitoring and Pollution Control, Nanjing, 210044, P. R. China. E-mail: leileixu88@gmail.com; chenmdnuist@163.com*

[b]*College of Light Industry and Food Engineering, Nanjing Forestry University, Nanjing 210037, P. R. China*

[c]*Jiangsu ShuangLiang Environmental Technology Co., Ltd, Jiangyin, 214400, P. R. China*

[d]*School of Material Science and Engineering, University of Jinan, Jinan, 250022, P. R. China*

† These authors contributed equally to this work.

catalytic activity toward CO oxidation. However, they are extremely restricted in wide and large-scale application due to the high price and scarcity. Thus, it is very important to design and explore the low-cost catalysts with identical catalytic performance to the noble metals. It was reported that various transition metal oxides (Co_3O_4,[20,21] CuO,[22] MnO_2,[23] and CeO_2 (ref. 24)) performed excellent catalytic activity for CO oxidation in the past decades. Among them, MnO_2 has been extensively investigated due to various advantages, such as low price, environmental friendliness, and relatively high activity.[25,26] With the continuous studies on MnO_2 based materials, it has been found that MnO_2 based catalysts usually perform good oxidation activities for the VOCs, such as formaldehyde, toluene, benzene, dimethyl ether, *etc*. Besides, the catalytic oxidation ability of MnO_2 can be greatly improved through crystal facet exposure engineering and regulating the loading methods.

Compared with the traditional bulk MnO_2, the nanostructured MnO_2 materials usually perform better physiochemical characteristics, such as the higher specific area, lower density, and more adjustable chemical nature. Furthermore, various studies have shown that MnO_2 with nanowire morphology usually perform high surface areas and strong metal–support interactions.[27–31] Therefore, the nanowire is the dominant morphology among the MnO_2-based nanostructured materials. Compared with MnO_2 nanorods, MnO_2 nanowires commonly possesses much more adsorbed surface oxygen, greater reducibility, higher specific area, and lower Mn–O bond strength, accounting for the better catalytic performances in the catalytic combustion of dimethyl ether[27] and plasma catalytic oxidation of toluene.[28] Saputra *et al.*[29] found that MnO_2 nanowire displayed much higher activity than the MnO_2 nanorod and nanofiber counterparts in activating oxygen ketones to degrade phenol. In addition to this, compared with rod-shaped and tubular MnO_2, the MnO_2 nanowire as the support behaved stronger interaction with Ag and displayed the much higher reactivity of toluene oxidation.[30] The α-MnO_2 nanowire also displayed the best catalytic activity toward gaseous benzene oxidation among the MnO_2-based nanomaterials with different morphologies (*e.g.*, wire and rod-like α-MnO_2, β-MnO_2 microrods) even after decorating Co_3O_4 nanoparticles.[31]

In recent years, more and more advanced and important materials have been developed for the applications of MnO_2-based nanomaterials in the removal of environmental pollutants,[32,33] biosensing,[34] theranostic,[35] especially in the field of electrochemistry.[36–38] For example, Li *et al.*[37,38] synthesized α-MnO_2 nanowires with outstanding circulation stability, demonstrated rate performance, and high specific capacitance for supercapacitor electrode. Therefore, the previous reviews of MnO_2-based nanomaterials were mainly focused on their applications in electrochemistry.[39–43] However, there were few reviews paid close attention to their environmental applications. Yang *et al.*[44] systematically summarized the environmental applications of MnO_2-based materials. But they did not specially highlight the unique advantages of MnO_2-based nanowire materials, which have been considered as the basic assembly unit of two-dimensional or three-dimensional

structure complex/heterostructure materials of MnO_2 (ref. 45) and normally have higher catalytic activity compared with MnO_2-based nanomaterials in other morphologies.[27–30] Meanwhile, the previous discussions about MnO_2-based nanowire materials were very scattered and their applications were mainly focused on the topic in the field of the electrochemistry. There has been few comprehensive reviews targeting the applications of MnO_2-based nanowire materials in the field of environmental catalysis. A systematic overview of frontier scientific research on the modulation of MnO_2-based nanowire materials for environmental catalysis application is urgent for the rational design and fabrication of high-efficiency MnO_2-based nanowire materials. Therefore, this review comprehensively summarizes the synthesis methods of MnO_2-based nanowires, such as hydrothermal, reflux, sol–gel, template method, *etc.*, and analyses the effects of various influencing factors, such as the crystalline phase structure, crystal facet, morphology, doping, and loading, on the performances of catalytic oxidation of CO, VOCs, and other environmental pollutants. In addition, the latest research progresses of MnO_2-based nanowire materials in the field of environmental catalysis are also covered in this review. With the in-depth research on MnO_2-based nanowire materials, their environmental applications have been greatly improved. However, there is still big gap between the theoretical study and practical application. Therefore, it is of great necessity to summarize the recent progresses for better understanding the real surface reaction mechanism, which will promise the future environmental application in the fields of catalytic oxidation, combustion, purification, and other related research fields.

2. Synthesis of MnO_2-based nanowires

There are various preparation methods of MnO_2 nanomaterials, such as the liquid phase precipitation method,[46,47] reflux method,[48] electrodeposition method,[49] hydrothermal method,[50–53] sol–gel method,[54,55] template method,[56] thermal decomposition method,[57] and so on. As a result, the phase structures and chemical characteristics of MnO_2 nanomaterials fabricated by different methods will be completely different. Similarly, the synthesis of MnO_2-based nanowires also mainly employs the hydrothermal method, reflux method, sol–gel, and template method. Herein, the synthesis method, reaction condition, morphology parameters, and structural properties of MnO_2-based nanowires have been summarized in Table 1.

2.1 Hydrothermal synthesis method

The hydrothermal synthesis of MnO_2-based nanowires mainly involves oxidation–reduction reaction of MnO_4^- and/or Mn^{2+} or the phase transition of MnO_2 precursor. The hydrothermal method usually involves several key parameters, including the reagent amount, reaction time, hydrothermal temperature, pH, and so on. Therefore, the MnO_2-based nanowires with different phase structures can be synthesized in a precisely controllable way by tuning these key parameters in the hydrothermal process.

RSC Advances

Table 1   The preparation method, raw materials, synthesis parameter, and the resultant structural properties of the MnO_2-based nanowires

MnO_2 nanowire	Preparation method	Raw materials	Synthesis temperature (°C)	Synthesis time (h)	Length	Diameter (nm)	BET (m² g⁻¹)	Reference
α-MnO_2	Hydrothermal method	$MnSO_4 \cdot H_2O$, $KMnO_4$	150	12	2.5 μm	20–40	61.0	82
	Hydrothermal method	$KMnO_4$, NH_4Cl	200	48	Several μm	100–200	53.1	61
	Hydrothermal method	$MnSO_4 \cdot H_2O$, $(NH_4)_2S_2O_8$	140	12	0.4–5 μm	5–20	148.0	29
	Hydrothermal method	δ-MnO_2, H_2SO_4	100	24	250–500 nm	30–60	93.1	27
	Hydrothermal method	$KMnO_4$, CH_3COOH	140	12	6–10 μm	30–60	39.9	83
	Reflux method	δ-MnO_2 nanosheets	80–90	90–120	>10 μm	20–30	53.2	58
	Sol–gel template method	AAO template, Mn$(CH_3COO)_2$, citric acid	400	12	500–700 nm	70	—	54
β-MnO_2	Hydrothermal method	$MnSO_4 \cdot H_2O$, $(NH_4)_2S_2O_8$	140	12	1.5–2.5 μm	60–100	55.7	84
	Hydrothermal method	Mn$(NO_3)_2$, O_3	200	8	2–5 μm	6–12	73.5	58
γ-MnO_2	Hydrothermal method	$MnSO_4 \cdot H_2O$, $(NH_4)_2S_2O_8$	90	24	—	—	—	85
δ-MnO_2	Hydrothermal method	$MnSO_4 \cdot H_2O$, $KMnO_4$	240	24	—	—	—	
α-MnO_2-100	Hydrothermal method	$MnSO_4 \cdot H_2O$, $(NH_4)_2S_2O_8$, $(NH_4)_2SO_4$, KNO_3	120	20	Several μm	15–20	87.9	86
α-MnO_2-110	Hydrothermal method	$KMnO_4$, $(NH_4)_2SO_4$	180	24	—	45–50	119.5	
	Hydrothermal method	$KMnO_4$, $(NH_4)_2C_2O_4 \cdot H_2O$	180	24	100–500 nm	10–50	—	87
α-MnO_2-210	Hydrothermal method	$MnCO_3$, HNO_3, $(NH_4)_2S_2O_8$, H_2SO4	140	2	100–500 nm	10–50	—	
α-MnO_2-310	Hydrothermal method	$KMnO_4$, $(NH_4)_2SO_4$	180	24	100–500 nm	10–50	—	
	Hydrothermal method	$KMnO_4$, $(NH_4)_2C_2O_4$	180	24	Several μm	15–20	135.3	86

DeGuzman et al.[50] pointed out that pH and temperature could affect the final phase structure of MnO_2 in the synthesis of fibrous α-MnO_2 nanomaterials and α-MnO_2 would transit into β-MnO_2 when the temperature was kept above 120 °C. However, Wang et al.[51] found that the effects of pH and temperature were not significant. In their study, 1D MnO_2 nanomaterials with different phase structures could be obtained in a wide temperature range (100–180 °C) just by varying the molar ratio of raw reactants ($KMnO_4$ and $MnSO_4$) without adjusting the pH (~2.5) of the system. Besides, the type of the raw reactants greatly determines the hydrothermal reaction temperature of preparing the α-MnO_2 nanowire. For example, the optimal hydrothermal temperature was located between 120 °C and 160 °C when using $KMnO_4$ and $MnSO_4 \cdot H_2O$ as raw materials;[58–60] whereas, the optimal hydrothermal temperature was 200 °C when using $KMnO_4$ and NH_4Cl as the precursors.[61–63] The effect of pH on the crystalline phase structure of the final product was also largely derived from the ion concentration as the tunnels of different MnO_2 crystal forms have different sizes and need different amounts of cations to stabilize.[64] Zhang

et al.[53] showed that the phase structure of MnO_2 and the aspect ratio of the final product were greatly depended on the concentration of ions in the reaction system, especially K^+. Because the high concentration of K^+ could be used as the effective template, which was more conducive to the synthesis of α-MnO_2 nanowire.[53] Wang et al.[51] believed that the layer structure of δ-MnO_2 tended to curl under the high temperature and pressure, which was considered as the determinant step for the formation of 1D nanostructures of MnO_2. Zhang et al.[53] also indicated that prolongating hydrothermal time could drive the self-assembly of α-MnO_2 into bundles and then transform into β-MnO_2. Therefore, the possible synthesis route of MnO_2-based nanostructures was described in Fig. 1. First, the MnO_x units appear in the solution and the δ-MnO_2 with the layer structure is then formed through a series of condensation reactions. δ-MnO_2 tends to curl under high temperature and high pressure. When K^+ concentration is high, α-MnO_2 can be formed; otherwise, β-MnO_2 can be formed. With the prolonging of hydrothermal time, the [2 × 2] tunnel structure of α-MnO_2 directly collapses into the [1 × 1] tunnel structure of β-MnO_2.[53] Wei
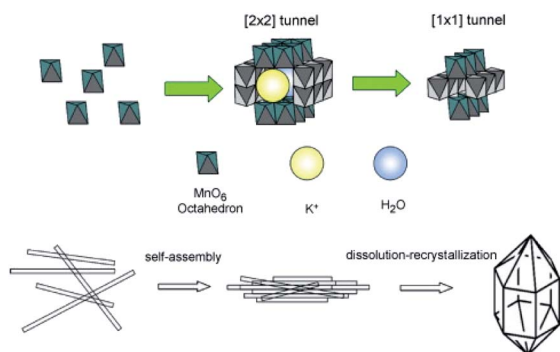
Fig. 1 Schematic illustration of the self-assembly of α-MnO$_2$ nanowires into bundles and their subsequent phase transformation to β-MnO$_2$ microcrystals under prolonged hydrothermal conditions. Reproduced by Zhang et al.[53] with permission from Elsevier.

et al.[52] studied the hydrothermal synthesis of MnO$_2$-based nanowires through the phase transition of granular MnO$_2$ precursor. They synthesized α-MnO$_2$ and β-MnO$_2$ single crystal nanowires by the hydrothermal treatment of γ-MnO$_2$ at different temperatures. This method not employing catalysts or templates could be easily reproduced. Therefore, the hydrothermal synthesis of different crystal types of MnO$_2$ nanowires with potential application prospects in large-scale could be realized.

Generally, the hydrothermal method of preparing MnO$_2$-based nanowire has various advantages, such as high product purity, excellent dispersion, good crystallinity, uniform morphology, etc. Besides, the preparation conditions are simple and the fabrication time is short. Therefore, the hydrothermal method has been widely used for the synthesis of MnO$_2$-based nanowires. However, the hydrothermal method is usually limited by the capacity of the reaction system, so it is not suitable for the large-scale industrial production. Furthermore, the tightness of the reaction system will bring safety hazards.[65]

2.2 Reflux method

The reflux is a kind of wet chemical synthesis method that does not require high-temperature calcination, and directly synthesizes nanomaterials with uniform particle size and high activity. The reflux method is suitable for the large-scale synthesis of MnO$_2$ nanowires owing to various advantages, such as simple operation and mild reaction conditions. Kijima et al.[66] synthesized MnO$_2$ with three different phase structures (α-, β-, and γ-) by the acid digestion of Mn$_2$O$_3$ under reflux conditions. The type of polymorph of MnO$_2$ products was strongly dependent on the reaction temperature, type of acid used, and the concentration. When H$_2$SO$_4$ was used as the acid, the α-MnO$_2$ was inclined to form at higher H$_2$SO$_4$ concentrations and lower reaction temperatures. In contrast, the β-MnO$_2$ was obtained at lower H$_2$SO$_4$ concentrations and higher reaction temperatures. The γ-MnO$_2$ were formed at intermediate conditions. When HNO$_3$ was used as the acid, only the β-MnO$_2$ and γ-MnO$_2$ could be formed. The α-MnO$_2$ could not be obtained in the HNO$_3$ solution. Compared with γ-MnO$_2$, the β-MnO$_2$ formation

usually demanded higher reaction temperatures (>80 °C) and higher concentrations of HNO$_3$ (>10 mol L^{-1}).[66] Chen et al.[67] synthesized transition metal doped α-MnO$_2$ nanofibers by the reflux method. Compared to the pristine MnO$_2$, metal cation doped MnO$_2$ materials had slightly higher surface areas and pore volumes, especially when the dopant content was relatively high. Jin et al.[68] synthesized γ-MnO$_2$ homogeneous nanofiber with the length of $\sim$1 μm and the diameter of 50 nm by refluxing and used it as the catalyst for catalysing the atmospheric oxidation of toluene with molecular oxygen. Sinha et al.[65] prepared δ-MnO$_2$ nanosheets by the reflux method and further deepened the morphological evolution and shape transformation into ultra-long α-MnO$_2$ nanowires with extremely high purity by reflux. The length of the nanowire was observed to exceed 10 μm. The detailed preparation process and SEM results are shown in the Fig. 2. The reflux method also has the advantage of low chemical cost and avoids using autoclaves under harsh hydrothermal reaction conditions. As a result, the high-quality α-MnO$_2$ nanowires could be generated without using catalysts and stencils. The reflux method provides a promising preparation method of α-MnO$_2$ nanowires in large scale.[65] May et al.[69] synthesized α-MnO$_2$-based nanowires and further studied the effect of doping methods on low-temperature CO oxidation of CuO/α-MnO$_2$ catalysts based on the nitric acid reflux method of Uematsu et al.[70]

2.3 Sol–gel method

As for the sol–gel method, it employs the metal alkoxides or inorganic salts as precursors to achieve gelation through continuous hydrolysis and polycondensation processes. Then, the gel experiences the heat, and other subsequent treatments to obtain the final target product. The sol–gel synthesis of nanostructured MnO$_2$ commonly includes various combinations of hydrated metal cations, such as manganese acetate (MnAc$_2$) and citric acid,[71] MnAc$_2$ and n-propyl alcohol,[54] tetrabutylammonium permanganate and methanol,[72] and KMnO$_4$
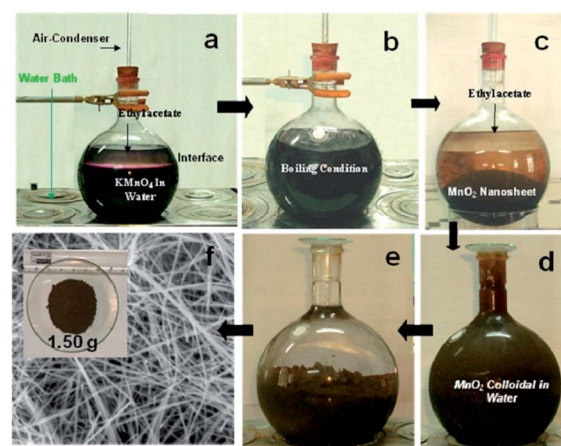

Fig. 2 Preparation of gram level α-MnO$_2$ nanowires from aqueous KMnO$_4$/ethyl acetate biphasic system and their different stages (a–f) in digital/FESEM images. Reproduced by Sinha et al.[65] with permission from ACS.

and fumaric acid $(C_4H_4O_4)$.[73,74] The structures of the obtained MnO_2 are strongly depended on the molar ratio between the $KMnO_4$ and the organic reducing agents.[75] For example, the 3 : 1 reactant ratio of $KMnO_4$ to glucose favoured the crypto-melane (2×2 tunnel) synthesis, while the 5 : 1 ratio generated the layered birnessite-type material.[72] Hastuti *et al.*[74] synthe-sized irregular spherical α-MnO_2 particles by the sol–gel method and discovered that transition metal (Fe^{3+}, Cu^{2+}) doping did not affect the phase structure but only changed the lattice param-eters and morphology of the final product. Hashem *et al.*[76] prepared the α-MnO_2 materials by redox reaction of $KMnO_4$ and ascorbic acid using the sol–gel method. The morphology of the final sol–gel samples were long needles with uniform diameter of ~15 nm and average length of ~0.8 μm, and further aggre-gated to urchin-like balls. Hashemzadeh *et al.*[71] prepared γ-MnO_2 polymorph using the manganese acetate and citric acid as the raw reagents in the sol–gel way. The obtained γ-MnO_2 polymorph was composed of particles with surface covered with needle-like nanorods. The researches have demonstrated that the sol–gel method could prepare 1D nanostructure MnO_2 nanowire with different morphologies. Ghorbani *et al.*[77] successfully synthesized MnO_2 nanowires with 45 nm in diameter using simple precursors, such as $KMnO_4$ and $NaNO_3$, by sol–gel method. They found that the optimal annealing temperature for achieving crystalline structure and nanowire morphology was 600 °C. Chin *et al.*[78] successfully prepared MnO_2 nanowires *via* the self-assembly of MnO_2 nanoparticles using the sol–gel method with $KMnO_4$ and $Mn(ClO_4)_2$ as the precursors. The microstructure and morphology of sol–gel derived MnO_2 nanowire were affected by the synthesis condi-tions and post synthesis heat treatment. Acidic pH value (pH 5.7) and calcination temperature at 300 °C were effective on achieving nanowire morphology and high surface area. Liu *et al.*[79] synthesized wire-like ion sieve $MnO_2 \cdot 0.5H_2O$ with about 50–200 nm in diameter and 0.5–2 μm in length using the sol–gel method. The ion sieve $MnO_2 \cdot 0.5H_2O$ nanowire had excellent adsorption performance for lithium extraction in seawater system and had a good application prospect. Furthermore, the combination of sol–gel and template has been considered as a better way to synthesize highly-ordered MnO_2-based
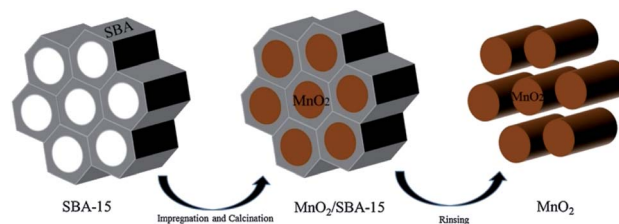

Fig. 4   Schematic representation of the preparation of MnO_2 by SBA-15 template. Reproduced by Zhang *et al.*[80] with permission from Elsevier.

nanowires than the sol–gel itself.[54,55] As shown in Fig. 3, Tang *et al.*[55] used CTAB as the surfactant to obtain highly dispersed ultrafine MnO_2 nanowires with the diameter of only 7 nm by the template directed sol–gel template method.

2.4   Template method

The template method has been considered as a common method for preparing nanomaterials by employing various structure directing agents or templates in recent years. Nano-materials with ordered structures are generated through the guidance of the template in the form of self-assembly by using the organic molecules as template agents. For example, Wang *et al.*[54] successfully prepared α-MnO_2 nanowire with the diam-eter of about 70 nm and the length between 500 nm and 700 nm using the sol–gel template method. The length and diameter of the nanowires greatly depended on the pore size and thickness of the employed AAO template. Gu *et al.*[56] used mesoporous silica SBA-15 as the hard template to prepare highly ordered array of mesoporous β-MnO_2 nanowires by the nano-casting method. Fig. 4 shows the schematic representation of the preparation of MnO_2 by using the SBA-15 as the template.[80]

The morphology of materials synthesized by the template method can be tunable by the choice of the template. However, the use of templates obviously increases the production cost. Therefore, reducing the costs of the templates is still an important concerned issue. Wang *et al.*[81] fabricated hierarchical MnO_2 microfibers by using cotton as the template and $KMnO_4$ as the precursor. In comparison with other templates, biolog-ical materials are "green" and easy to obtain, and the morphology of cotton fiber is more uniform than other kinds of plant fibers. This green, sustainable, and low-cost biotemplat-ing method can be extended to the synthesis of MnO_2-based nanowires and other metal oxide materials in the view of economical concern.

3.   The factors affecting the catalytic performances of MnO_2 nanowires

3.1   Phase structure

The $[MnO_6]$ octahedral unit is the basic building block for crystalline-phase MnO_2 materials. As shown in Fig. 5, when $[MnO_6]$ octahedral units are linked in different ways, the MnO_2 can form a variety of polymorphs, such as α-, β-, γ- and δ-MnO_2.[88–90] Studies have found that the phase structure can
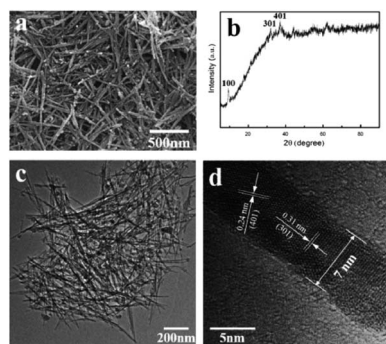

Fig. 3   (a) SEM image, (b) XRD pattern, (c) and (d) TEM images of MnO_2 nanowire prepared by sol–gel approach. Reproduced by Tang *et al.*[55] with permission from Elsevier.
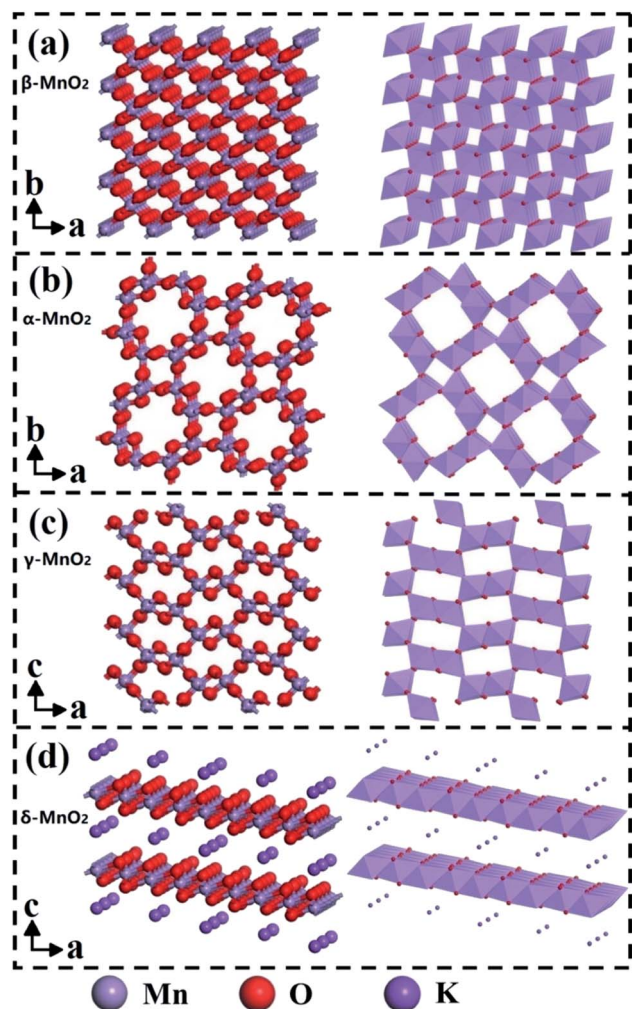

Fig. 5   Ball-stick and polyhedron representations of (a) β-, (b) α-, (c) γ- and (d) δ-MnO₂. Reproduced by Li *et al.*[91] with permission from Elsevier.

significantly affect the catalytic activity of MnO_2, and both α-MnO_2 and δ-MnO_2 are the dominant phase structures of MnO_2-based catalytic nanomaterials.[91–94]

Specifically, α-MnO_2 occupies more space than β-, γ-, and δ-MnO_2 due to the double tunnel structure of $[2 \times 2]$ and $[1 \times 1]$. As a result, it obtains more adsorption sites for the reactants (such as CO and VOCs) than other phases. At the same time, the existence of surface open pore structure can also increase the surface area of α-MnO_2 nanowires, thereby providing abundant oxygen adsorption sites for the reactants.[92] In addition, α-MnO_2 also has the weakest Mn–O bond strength among these crystalline phase structures, which could provide the lattice and absorbed oxygen during the oxidation reaction. Therefore, α-MnO_2 performs much better activity than other phase structures in catalytic reactions, such as CO oxidation,[26] O_3 catalytic degradation,[93] plasma oxidation of toluene,[28] and degradation of phenol by activating oxyketone.[29]

δ-MnO_2 is composed of $[MnO_6]$ octahedrons shared by the double layer edges. The special layer structure makes it easy for

toluene molecule to absorb on the surface of δ-MnO_2 and thereby behaves excellent activity in the catalytic oxidation of toluene.[91] As the comparison, the α-MnO_2 performs weaker toluene oxidation activity due to the lower content of Mn^{4+} and lattice oxygen.[91] Besides, δ-MnO_2 has also been proved to be the best crystalline phase structure for low-temperature catalytic oxidation of formaldehyde.[94]

β-MnO_2 with $[1 \times 1]$ tunnels have the most stable redox ability among these four phase structures. Besides, the surface area of β-MnO_2 nanowire materials is usually the smallest among the four phase structures, which will greatly hinder the adsorption and activation of the reactants and oxygen. As a result, it usually performs the lowest activity in the catalytic oxidation of CO and VOCs. The $[2 \times 1]$ and $[1 \times 1]$ tunnel structures of γ-MnO_2 have relatively mediocre catalytic activity in the oxidation of CO and VOCs.

3.2 Crystal facet

Studies have shown that the catalytic activities toward specific substances can be significantly improved by synthesizing nanomaterials with a high proportion of exposure specific crystal facets.[95–97] Recently, more and more studies have paid attention to the influence of specific crystal facets on their catalytic effects, such as TiO_2,[95] Fe_2O_3,[96] CeO_2 (ref. 97) and Co_3O_4,[20] because they are closely related with the final catalytic performances. Meanwhile, the great progresses have been made in the application of specific crystal facet of MnO_2-based nanowires to the catalytic oxidation of VOCs, such as formaldehyde,[86] methylmercury[93] and toluene,[87] *etc.*

Theoretically, the reactivity and activity of crystal faces are proportional to their surface energy. Therefore, the crystal facets with higher surface energies are usually more reactive in heterogeneous reactions.[98] Many studies have been carried out on the α-MnO_2 nanowires because α-MnO_2 has highest activity among the four phase structures of MnO_2-based nanowires. The characteristic crystal facets of α-MnO_2 generally include (310), (100), (110), and (210). Among them, (310) crystal facet possesses the highest surface energy, which is beneficial to the formation of oxygen vacancy. Thereby, the adsorption and activation of O_2, H_2O (ref. 86) and O_3,[93] *etc.*, could be promoted. As a result, (310) crystal facet performs obviously better activities on the oxidation of formaldehyde and the ozonation of methylmercury than (100) and (110) counterparts (see Fig. 6). Rong *et al.*[86] reported that the 310-α-MnO_2 could completely convert 100 ppm formaldehyde to CO_2 at 60 °C, which was even better than some silver-based catalysts.[99,100] As shown in Fig. 7, the (310) facets with high surface energy could not only facilitate adsorption/activation of O_2 and H_2O but also be beneficial to the generation of oxygen vacancies, which resulted in significant enhancement of HCHO oxidation activity. He *et al.*[93] reported that the 310-α-MnO_2 could completely remove 70 ppm of methyl mercaptan within 20 minutes at room temperature. However, crystal planes with higher surface energy usually disappear in most crystals with the fast growth and the thermodynamically stable crystal planes would preferentially dominate the surface to minimize the total surface energy of the
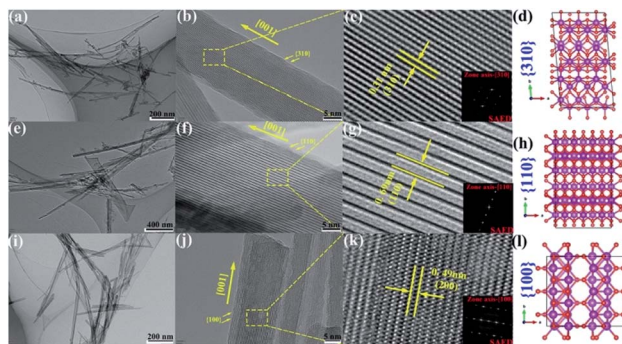
Fig. 6 TEM and HRTEM images of (a–c) α-MnO_2-310, (e–g) α-MnO_2-110, and (i–k) α-MnO_2-100. Atomic structure of the (d) {310}, (h) {110}, and (l) {100} surface of α-MnO_2. Small (red) spheres are oxygen and large (purple) are manganese. Reproduced by Rong et al.[86] with permission from ACS.
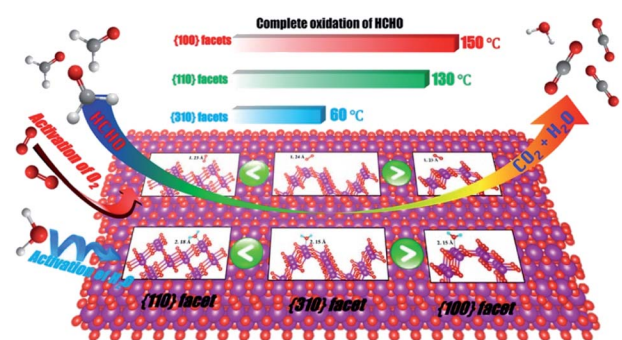

Fig. 7 α-MnO_2 nanowires with (100), (110) and (310) facets for HCHO oxidation. Reproduced by Rong et al.[86] with permission from ACS.

crystal.[86] Meanwhile, Huang et al.[87] found that (210) crystal plane with the lower surface activation energy (24.75 kJ mol^{-1}) showed better catalysis activity and stability for toluene than (110) and (310) crystal plane. The lower surface activation energy accelerated the activation and oxidation of toluene. The alternating arrangement of Mn–O atoms in the electronic structure also speeds up the oxidation and desorption of intermediate products, thus exhibiting excellent activity.

All in all, the specific VOCs oxidation reaction mechanism on the MnO_2-based nanowires is the key to improving the oxidation ability of MnO_2-based nanowire catalyst to VOCs through crystal facet engineering. It is also greatly necessary to strengthen the research on the mechanism of catalytic oxidation of VOCs because of the specific advantages of each crystal facet of MnO_2-based nanowires.

3.3 Morphology

As well known, the physiochemical properties of MnO_2 with different morphologies are often different.[101,102] The common one-dimensional structure of MnO_2 includes nanorods, nanotubes and nanowires. Among these morphologies, the MnO_2 nanowires occupies an important place. Because one-dimensional nanowires can be used as the basic assembly unit of two-dimensional or three-dimensional structure

materials.[45] Furthermore, the composite materials with novel structures and properties can be facilely prepared on the basis of them.

One of the basic parameters greatly affecting the performance of nanowires is the length or aspect ratio. For example, the photocatalytic performance of $W_{18}O_{49}$ nanowires is greatly affected by its aspect ratio;[103] the dielectric properties of $BaTiO_3$ nanowires also have close relationship with its length.[104] Therefore, the performance of the nanowire can be tuned by controlling the length or aspect ratio. Liao et al.[105] investigated the influence of the length of α-MnO_2 nanowires on the catalytic combustion performance of dimethyl ether. The results revealed that the length of the nanowires would affect the redox property of α-MnO_2 and the final catalytic combustion performance of dimethyl ether. Among them, α-MnO_2 nanowires with medium length (4–8 μm) possessed the best catalytic performance with ignition temperature at 167 °C and the complete combustion temperature at 240 °C. The 20 h life test demonstrated that the sample behaved good stability without deactivation.[105] Li et al.[91] prepared three kinds of δ-MnO_2 with different crystallinities and morphologies. The complete toluene conversion was achieved at 250–275 °C for δ-MnO_2 and the toluene conversion efficiency of δ-MnO_2 would be promoted with the decrease of crystallinity degree and particle size. Although the effect of the crystallinity and morphology were not as significant as the phase structure, they indeed greatly affected the activity of MnO_2 in the catalytic oxidation of toluene.

3.4 Metal loading and doping

The metal loading and doping are two common used modification methods when preparing catalyst. Both of them could significantly improve the catalytic activity of the MnO_2-based nanowire. The loading method could highly and uniformly disperse metal or metal oxide on the surface of catalytic support and the catalysts with higher activities could be achieved due to the formed strong metal-support interactions.[106] The doping method is to replace a small portion of the second metal cations in the host metal oxide with different cations can greatly change the chemical bonding on the surface of the host metal oxide, thereby improving its catalytic performance.[107] The active site in such catalytic system could be either the oxygen atoms near the dopant or the dopant itself. As a result, the activity of MnO_2-based nanowire can be further improved by dispersing more active ingredients on its surface.

The studies related to the metal modification of MnO_2 usually starts with the loading of noble metals, such as Au and Ag. For example, Gu et al.[56] loaded Au nanoparticles on α-, β-MnO_2 nanowires and developed Au/MnO_2 catalyst with extremely high activity and stability for CO oxidation at low temperature. The Au/α-MnO_2 nanowire catalyst showed the CO conversion of around 37% at −90 °C. As the temperature increased, the CO conversion increased rapidly to 90% below −60 °C, and slowly reached 100% at around −34 °C. The low-temperature (−85 °C) CO oxidation rate over this catalyst (2.8 mol_{CO} h^{-1} g_{Au}^{-1}) was almost 30 times higher than that of the Au/Mn_2O_3.[108] Qin et al.[109] investigated the

toluene oxidation activity over the α-MnO$_2$ nanowires supported catalysts with different Ag loading amounts, which greatly affected the toluene oxidation performance. As could be seen in Fig. 8, 4% Ag/MnO$_2$ catalyst performed the highest activity of the toluene oxidation and the lowest apparent activation energy (45.5 KJ mol^{-1}) among Ag/MnO$_2$ catalysts. They found that 4% loading of Ag could greatly facilitate the adsorption of toluene molecules and optimally increase the activation capacity of MnO$_2$ lattice oxygen between the interface of Ag and MnO$_2$, thereby increasing the reaction rate and promoting deep oxidation between toluene and lattice oxygen.[109] Apart from the loading of noble metals, Sadeghinia et al.[84] reported that the catalytic activity of CO oxidation could be enhanced by loading the α-MnO$_2$ nanowires with different contents of CuO. The 30% CuO/α-MnO$_2$ catalyst could achieve the complete CO conversion at about 100 °C, which was nearly 100 °C lower than pristine α-MnO$_2$ nanowire. May et al.[69] further confirmed that the loading of CuO by the deposition precipitation (DP) method would make the one-dimensional nanostructure of MnO$_2$ with more excellent CO catalytic oxidation activity than the incipient wetness impregnation. Specifically, the most active 5CuO/MnO$_2$ could achieve 80% CO conversion rate at 30 °C.

In view of the excellent performance of CuO loaded MnO$_2$-based nanowire catalysts,[84] the researches gradually focused on the transition metals doped catalysts because of the low cost and abundant availability. Lambert et al.[110] reported that the catalytic activities of α-MnO$_2$ nanowires doped with Cu and Ni

were significantly better than that of the pristine α-MnO$_2$ nanowires. Gao et al.[61] investigated the effects of doping Fe, Co, Ni, and Cu transition metals on the catalytic performance CO oxidation of α-MnO$_2$ nanowires. As shown in Fig. 9, the appropriate amount of transition metal doping would not apparently change the morphology, phase structure, and specific surface area of MnO$_2$ nanowires. As could be observed in Fig. 10, the CO oxidation activities of the transition metal doped α-MnO$_2$ nanowires were also significantly increased. Among them, Cu doped α-MnO$_2$ nanowires showed the best CO oxidation activity. The density functional theory calculations further revealed that doping Cu could more easily form oxygen vacancies in MnO$_2$ than doping Fe, Co, and Ni, which was the determinant of the CO oxidation reaction rate. Therefore, the Cu-doped nanowires performed the higher CO oxidation catalytic activity than those for noble-metal-free catalysts, such as Cu-substituted Co$_3$O$_4$,[111] Cu-doped CeO$_2$,[112,113] CuO/Al$_2$O$_3$.[114] In addition, Jampaiah et al.[62] also studied the MnO$_2$ nanowires doped with two transition metals. Their results showed that the Cu and Co doped MnO$_2$ nanowires could greatly improve the soot oxidation activity and its T$_{50}$ of soot conversion was as low as 279 °C. The advantage of two transition metals doped MnO$_2$ nanowires was that it enhanced the strong synergistic interaction between the transition metals. However, this study had shown that there was an upper limit for the amount of surface metal doping of MnO$_2$ nanowires. Because the original nanowire morphology would be damaged when the surface metal doping amount reached 20%.[62]

3.5 Interface effect

The interface effect derived from nanostructures plays an important role in enhancing the catalytic activity. It is widely
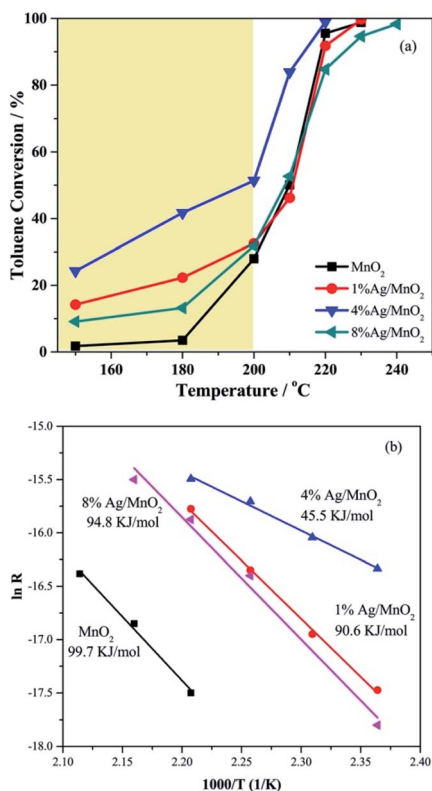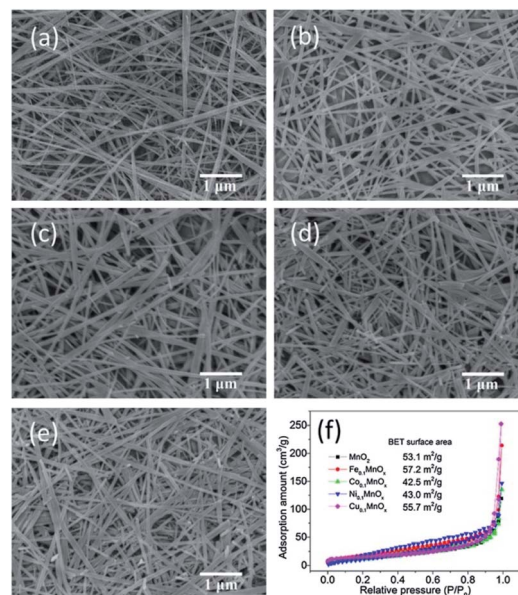

Fig. 8 (a) Catalytic performance of the catalysts for toluene oxidation; (b) Arrhenius plot of the reaction rate of the catalysts. Reproduced by Qin et al.[109] with permission from Elsevier.

Fig. 9 SEM images of (a) MnO$_2$, (b) Fe$_{0.1}$MnO$_x$, (c) Co$_{0.1}$MnO$_x$, (d) Ni$_{0.1}$MnO$_x$, and (e) Cu$_{0.1}$MnO$_x$ nanowires and (f) N$_2$ adsorption–desorption isotherms. Reproduced by Gao et al.[61] with permission from Elsevier.
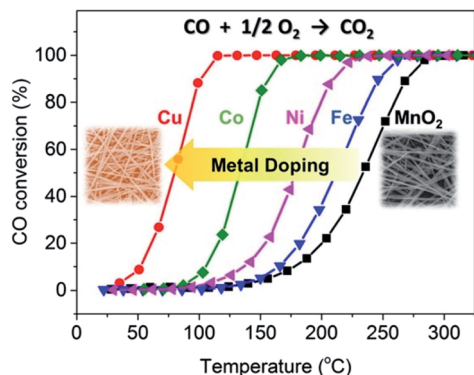
Fig. 10 CO oxidation activity tests of the MnO₂ and Fe-, Co-, Ni-, and Cu-doped MnO₂ catalysts. Reproduced by Gao *et al.*[61] with permission from Elsevier.

believed that multi-component metal oxides with coupling interfaces often exhibit better catalytic activity than single-component metal oxides.[115–119] For example, as regards the α-MnO₂@Co₃O₄ catalyst, the heterogeneous interface constructed by MnO₂ nanowires and Co₃O₄ nanoparticles could not only enhance the redox pair of Mn^{4+}/Mn^{3+} and Co^{2+}/Co^{3+} but also strengthen the adsorption of oxygen on the surface and accelerate the fluidity of oxygen. As a result, the catalytic activities of α-MnO₂@Co₃O₄ toward the oxidation of benzene[31] and toluene[120] were much better than that of pristine MnO₂ nanowires. The α-MnO₂ nanowire@Co₃O₄ could reduce the T_{90} of benzene oxidation to 247 °C (see Fig. 11) and the T_{90} of toluene conversion to 229 °C, which were 100 °C and 47 °C lower than that of the pure α-MnO₂ nanowire, respectively.[31,120] Deng *et al.*[121] successfully prepared the MnO₂ nanowire@NiO nanosheet core–shell hybrid nanostructure by uniformly decorating NiO nanosheets on α-MnO₂ nanowires. The obtained catalyst could achieve the complete oxidation of benzene at 320 °C, which was 60 °C lower than the pure MnO₂ nanowire. Ma *et al.*[122] prepared MnO₂@TiO₂ by immobilizing crystalline anatase TiO₂ on the surface of α-MnO₂ nanowire. The as-prepared MnO₂@TiO₂ exhibited much higher maximum adsorption capacity (105.3 mg g⁻¹) of the

radioactive element U(VI) than the pure MnO₂ (13.3 mg g⁻¹), illustrating that the performance of the surface-modified MnO₂ was greatly improved.

Homojunctions are junctions layer made of the same semiconductor materials.[44] It has been revealed that the construction of homojunctions could enhance the adsorbing and catalytic performance of the MnO₂ nanomaterials.[123,124] Zhou *et al.*[123] constructed α-MnO₂@δ-MnO₂ homojunction by loading layered δ-MnO₂ nanoflakes on the framework of α-MnO₂ nanotubes. The α-MnO₂@δ-MnO₂ homojunction integrated the exposed surfaces of the α-MnO₂ (100) surface and δ-MnO₂ (001) surface at the same time and displayed outstanding catalytic performance toward the oxidation of formaldehyde. The α-MnO₂ (100) surface was conducive to the adsorption and activation of oxygen molecules and the δ-MnO₂ (001) surface was favourable for the desorption of H₂O. The synergistic effect of the two surfaces significantly enhanced the catalytic activity for formaldehyde oxidation at room temperature. Huang *et al.*[124] synthesized the special two-phase structure MnO₂ catalyst simultaneously with α-MnO₂ and β-MnO₂ (α-MnO₂: β-MnO₂ = 1 : 1). As a result, toluene could be completely oxidized over the α@β-MnO₂ two-phase catalyst at about 205 °C, which was lower than the pure α-MnO₂ (220 °C) and β-MnO₂ (260 °C). Compared with the single-phase MnO₂, the α@β-MnO₂ with two-phase structure generated more abundant active interface and oxygen vacancy, thus promising enhanced catalytic performances.

4.   Application in catalytic oxidation

4.1   CO oxidation

CO is one of the most common atmospheric pollutants harmful to the health of human beings. Its capacity of binding to hemoglobin is about 210 times higher than O₂.[125] Therefore, the combination of CO and hemoglobin severely hinders the delivery of blood oxygen, which will cause the supply shortage of blood oxygen and further threaten the life safety. Given these drawbacks, the low-temperature catalytic oxidation of CO has been considered as one of the most important environmental catalysis
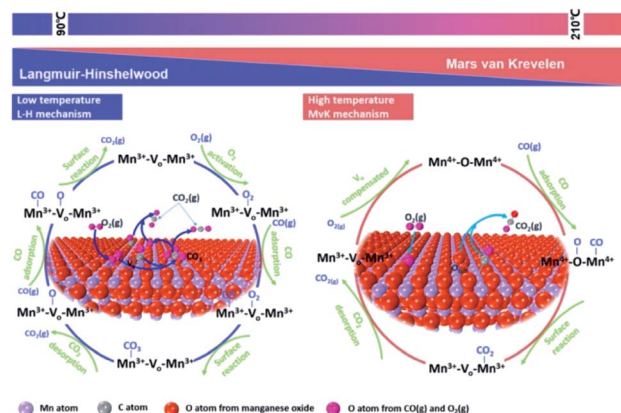

Fig. 11 Benzene oxidation activity tests of the 1D MnO₂@Co₃O₄ and 1D MnO₂ catalysts. Reproduced by Tang *et al.*[31] with permission from Elsevier.

Fig. 12 Proposed reaction mechanism of CO oxidation on metal oxide. Reproduced by Tian *et al.*[126] with permission from Elsevier.

processes. As shown in Fig. 12, the proposed reaction mechanism of CO oxidation on manganese oxide catalyst commonly abides by Langmuir–Hinshelwood reaction mechanism (L–H mechanism) at low temperature (<90 °C) and Mars-van Krevelen reaction mechanism (MvK mechanism) at high temperatures ($T > 190$ °C).[126] When the temperature is low (50–90 °C), gaseous O_2 are captured by oxygen vacancies and the active oxygen species (O_2^- or O_2^{2-}) could be formed. Subsequently, the adsorbed CO (CO–Mn^{3+}) tent reacts with active oxygen species to generate bidentate carbonate species, and then decompose into CO_2. Finally, the dissociated O species could be restrained by oxygen vacancies and react with the adsorbed CO to form CO_2 which follows the L–H mechanism. When the temperature is high ($T > 190$ °C), the surface lattice oxygen species can directly react with adsorbed CO to generate CO_2 and oxygen vacancies due to the activation of surface lattice oxygen species. Subsequently, the oxygen vacancy was refilled by gaseous O_2 and the redox cycle is completed by following the MvK mechanism. The T_{10}, T_{50}, T_{90}, T_{100} and BET of

MnO_2-based nanowire materials on the catalytic oxidation of CO and some VOCs have been summarized in Table 2.

Previous studies found that the crystalline phase structure could significantly affect the CO catalytic activity of MnO_2.[26,92,127] Liang *et al.*[26] synthesized four different crystalline MnO_2 nanooxides. They found that the order of activity for catalytic oxidation of CO was α ≈ δ > γ > β-MnO_2. Because the tunnel structure of [2 × 2] and [1 × 1] of α-MnO_2 could occupy more space to obtain more CO adsorption sites; whereas, other crystalline MnO_2 only involved β-MnO_2 with [1 × 1] tunnel, γ-MnO_2 with [2 × 1] and [1 × 1] tunnels, and δ-MnO_2 composed of [MnO_6] octahedrons shared by the double-layer edges. Another reason accounting for the enhanced catalytic CO oxidation performance of α-MnO_2 was that the elongated Mn–O bond length stemming from the distorted [MnO_6] units could benefit the cracking of the Mn–O bond, promoting CO oxidation.[26,127] As a result, α-MnO_2 could easily react with CO and thus further improved its catalytic performance.

Table 2 T_{10}, T_{50}, T_{90}, and T_{100} of MnO_2-based nanowire catalysts toward different catalytic substances

MnO_2 based nanowire material	BET (m^2 g^{-1})	Catalytic substance	T_{10} (°C)	T_{50} (°C)	T_{90} (°C)	T_{100} (°C)	Reference
α-MnO_2	31.3	CO	—	~180	~210	260	84
20% CuO/α-MnO_2	22.0		—	~75	~100	150	
Au/α-MnO_2	40.0		—	−83	−60	−34	56
α-MnO_2	53.1		~180	234	~275	~300	61
$Fe_{0.1}MnO_x$	57.2		~170	212	~260	~275	
$Co_{0.1}MnO_x$	42.5		~110	133	~160	~180	
$Ni_{0.1}MnO_x$	43.0		~140	178	~220	~260	
$Cu_{0.1}MnO_x$	55.7		50	80	—	100	
α-MnO_2	80.6		~80	~110	126	~155	127
β-MnO_2	55.7		~95	~150	169	~185	
Ag/α-MnO_2	64.2		~45	~75	90	~120	
Ag/β-MnO_2	40.0		~35	~65	80	~115	
α-MnO_2	51.1	Soot	492	547	602	—	62
5Co–MnO_2	50.2		436	513	567	—	
10Co–MnO_2	51.7		420	475	546	—	
20Co–MnO_2	50.7		479	528	586	—	
5Ni5Co–MnO_2	58.3		379	445	513	—	
5Cu5Co–MnO_2	59.4		368	431	485	—	
α-MnO_2	52.7	Benzene	243	301	345	~375	31
α-MnO_2@Co_3O_4	58.5		205	227	247	~265	
α-MnO_2	52.7		243	301	~350	380	121
α-MnO_2@NiO	88.9		233	273	~300	320	
α-MnO_2	—	Toluene	~186	~210	~220	~230	109
4% Ag/α-MnO_2	—		—	~195	~215	~220	
α-MnO_2	39.9		214	~230	237	~245	83
α-MnO_2-110	—		—	142	170	200	87
α-MnO_2-210	—		—	88	109	140	
α-MnO_2-310	—		—	130	170	200	
α-MnO_2	60.6		~240	264	276	~285	120
α-MnO_2@Co_3O_4	54.9		~205	220	229	~235	
α-MnO_2	93.1	Dimethyl ether	200	~230	274	~290	27
α-MnO_2(1 ~ 3 μm)	—		176	—	—	250	105
α-MnO_2(4 ~ 8 μm)	—		167	—	—	240	
α-MnO_2(6–10 μm)	—		170	—	—	250	
α-MnO_2-100	87.9	Formaldehyde	~80	125	~145	150	86
α-MnO_2-110	119.5		~50	100	~125	130	
α-MnO_2-310	135.3		—	35	~55	65	

In addition, various studies have been conducted to improve the catalytic activity of MnO_2-based nanowires for CO oxidation. In order to achieve this goal, effective strategies including element doping, surface engineering and combination with other active substances have been extensively conducted. Gao *et al.*[61] found that the hydrothermal doping of Cu would significantly increase CO oxidation activity (TOF = 9.1×10^{-3} s^{-1} at 70 °C) and water resistance of α-MnO_2 nanowires. As for γ-MnO_2, Zn-doped MnO_2 could achieve the 90% CO conversion at 160 °C and perform the best CO oxidation activity among Cu, Zn, Mg, Co, Ni, Ca, Al, Fe, and La-doped γ-MnO_2.[128] Besides, the surface engineering is considered as another effective method to improve the catalytic activity of MnO_2. Li *et al.*[92] synthesized α-MnO_2 with a large number of surface open cells through acid treatment. The open cells were rich in adsorption sites for O_2, thus enhancing the catalytic activity of MnO_2 for CO oxidation. Moreover, combining Au,[56] Ag,[127] CuO,[69,84] *etc.* with MnO_2 nanomaterials can effectively improve CO oxidation efficiency. Xu *et al.*[127] investigated the CO oxidation activity over the α-MnO_2 nanowires supported Ag based catalysts and the T_{90} of Ag/α-MnO_2 below 100 °C could be achieved. Although many studies have been carried out to enhance the catalytic activity of MnO_2 for CO oxidation and the complete CO conversion could be achieved at −34 °C,[56] the current research hotspot is still focused on the loading or doping noble/transition metals. The further explorations should be concentrated on the surface engineering or the rare earth metals modification.

4.2 Catalytic removal of VOCs

The volatile organic compounds (VOCs) typically refer to organic compounds with boiling points between 50 °C and 260 °C at atmospheric pressure (101.325 kPa) according to the World Health Organization.[129] Besides, most VOCs emitted into the atmosphere can cause the formation of secondary pollutants, such as tropospheric ozone, peroxyacetyl nitrate, and secondary organic aerosols.[130–132] Various means have been used to remove the VOCs, such as the physical adsorption,[133] catalytic oxidation,[134,135] photocatalytic degradation,[136,137] plasma catalytic oxidation,[138] and biological decomposition.[139] Among these strategies, the catalytic oxidation has been considered as one of the most effective ways owing to various advantages, such as high efficiency, less secondary pollutants, and low reaction temperature. As for the catalysts of VOCs oxidation, compared with precious metal catalysts, the transition metal oxides catalysts are considered to be more promising candidates owing to their low costs and excellent catalytic performances.[140] MnO_2 based nanomaterials are widely investigated as the effective catalysts and/or supports in the fields of pollutant removal, energy storage, and water treatment due to the excellent oxygen storage/release capacities, adsorption performances, and redox performances.[141]

4.2.1 Benzene. Benzene is extensively used in the fields of basic chemical and petrochemical industries. However, it is also harmful to human health at high risk. It is classified as the human carcinogen causing leukemia by the WHO.[129] Up to now, the supported noble metal based catalysts, such as Pt, Pd, Au,

Ag based catalysts,[142–145] are well known as the active catalysts for the oxidation of the benzene at low temperature. However, the development of the low-cost catalysts for the oxidation of benzene is in greatly urgent demand and the MnO_2 based catalysts are promising candidates due to facile availability.

Hu *et al.*[146] found that the order of catalytic activities on benzene combustion over MnO_2 with different phase structures was γ-MnO_2 > β-MnO_2 > α-MnO_2 > δ-MnO_2. The surface adsorbed oxygen species concentration and low temperature O_2 desorption of these manganese oxides were in good agreement with the sequence of their catalytic performance on benzene combustion. Besides, the strategies such as metal doping and loading have been investigated to improve the catalytic activities on benzene combustion over MnO_2. Liu *et al.*[147] found that the Ce^{3+} and Cu^{2+} doped of MnO_2 nanosheet could significantly improve the activity of MnO_2 for benzene decomposition. For the pristine MnO_2, benzene was hardly decomposed below 200 °C and only ~40% conversion was achieved at 400 °C. Whereas, as for the Ce–MnO_2 and Cu–MnO_2 catalysts, the benzene started to decompose around 100 °C and nearly all benzene could be removed around 250 °C. Moreover, the Cu–MnO_2 catalyst also exhibited high resistance to high-temperature deactivation and water resistance during continuous long-term testing. Recently, Ma *et al.*[148] synthesized the tungsten-doped MnO_2 (W–MnO_2) with excellent performance of the photo-assisted thermal catalytic oxidation/removal of benzene. They found that doping W could not only generate abundant oxygen vacancies in MnO_2, but also produce strong covalent interactions with adjacent O atoms through W–O bridge bonds, thereby promoting O_2 polarization and electron transference.

As for the metal loading, Ye *et al.*[149] prepared nanosized α-MnO_2-supported silver catalysts for benzene oxidation. They found that the 5Ag/MnO_2 catalyst performed the best activity of the benzene oxidation. Tang *et al.*[31] modified one-dimensional MnO_2-based catalysts (wire-like, rod-like α-MnO_2 and β-MnO_2 microrods) by the Co_3O_4 nanoparticles (see Fig. 13) and investigated them as the catalysts for benzene oxidation. They found that the modified MnO_2@Co_3O_4 composite exhibited better catalytic performance than the pristine MnO_2. The specific conversion efficiencies of the modified material to benzene abided by the order of α-MnO_2 nanowires > α-MnO_2 nanorods > β-MnO_2 nanorods. The reason for this could be attributed to the enhanced low-temperature reducibility and abundant active surface adsorption of oxygen derived from the heterogeneous hybrid interface.
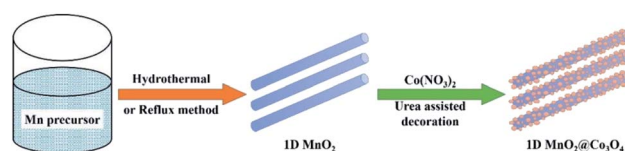

Fig. 13 Schematic process for the preparation of 1D MnO_2@Co_3O_4 hetero-nanostructures. Reproduced by Tang *et al.*[31] with permission from Elsevier.

4.2.2 Toluene. Toluene could directly threaten the human health and safety because of its carcinogenicity and teratogenicity.[150,151] Therefore, the effective removal method of toluene should be explored in great urgency considering the harmful effects of toluene on the human health and the strict environmental regulations. Cheng et al.[83] found that α-MnO_2 nanowires performed much higher catalytic activity than the commercial MnO_2 counterpart toward toluene combustion. The reason for this could be attributed to the enhanced surface oxygen mobility and surface area of α-MnO_2 nanowires, which were significantly better than the commercial MnO_2. The possible oxidation reaction mechanism of toluene over α-MnO_2 catalyst was summarized in Fig. 14. Firstly, toluene adsorbed on α-MnO_2 catalyst surface. The adsorbed toluene would be subsequently oxidized into benzyl alcohol by surface lattice oxygen. Meanwhile, the resultant oxygen vacancies could be supplemented by gas-phase O_2, and active oxygen species ($O_2/O_2^-/O_2^{2-}/O^-/O^{2-}$) would be formed.[86] The benzyl alcohol would be oxidized by active oxygen species into the benzaldehyde, and then further oxidized into the benzoic acid. Finally, the benzene ring would be destroyed by active oxygen species. After ring-opening, the unsaturated long chain enol and alkyne could be ultimately transformed into the CO_2 and H_2O quickly.[87]

It has been reported that the catalytic performances of the toluene oxidation over the MnO_2 nanomaterials were strongly related to the crystalline phase structures.[91,124,152] Li et al.[91] prepared MnO_2 with different crystalline phases (β-, α-, γ-, and δ-). The results showed that catalytic toluene oxidation activities followed the sequence of δ > γ > α > β-MnO_2. The morphology of the MnO_2 nanostructure also greatly influences the catalytic performance of the toluene oxidation. The previous study showed that the MnO_2 nanowire showed the most excellent toluene combustion catalytic activity (T_{100} = 220 °C) after loading silver among the MnO_2-based one-dimensional nanostructures (nanowire, nanorod, and nanotube).[30]

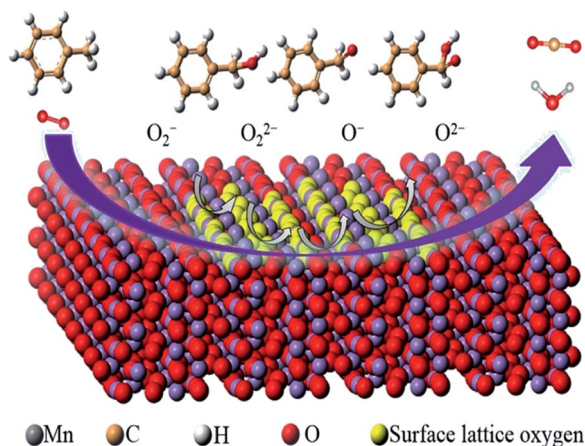Besides, the metal loading and doping can also greatly enhance the catalytic performance in toluene oxidation removal.[153,154] Dong et al.[153] found that the introducing Na^+ and Ca^{2+} into MnO_2 promised the higher catalytic activity for toluene oxidation than pristine MnO_2. Specifically, the Ca–MnO_2 catalyst exhibited the best catalytic activity (T_{90} = 215 °C) and possessed good water resistance. The outstanding catalytic performance of Ca–MnO_2 was closely related to the abundant acidic sites, high oxygen vacancy concentration, and the weak CO_2 adsorption capacity. Min et al.[154] found that transition metal (Ni and Co) doped α-MnO_2 and β-MnO_2 exhibited better catalytic performances in toluene oxidation removal owing to their lower crystallinities, more defects, larger specific surface areas, more oxygen vacancies, and better low-temperature redox ability than the pristine α-MnO_2 and β-MnO_2.

The catalytic performance of the toluene oxidation was also influenced by the interface between different metal oxides. Ren et al.[120] fabricated ZIF-derived Co_3O_4 grown in situ on 1D α-MnO_2 materials (as displayed in Fig. 15) and used it as the catalyst for toluene oxidation. They found that the α-MnO_2@Co_3O_4 could reduce the T_{90} of toluene conversion to 229 °C, which was 47 °C and 28 °C lower than those of the pure α-MnO_2 nanowire and Co_3O_4-b, respectively. The main reason for the enhanced catalytic activity could be attributed to the synergistic effect produced by the coupling interface constructed between α-MnO_2 and Co_3O_4. The specific reaction route of toluene oxidation on α-MnO_2@-Co_3O_4 catalyst could be illustrated as follows: toluene → benzoate species → alkanes containing oxygen functional group → CO_2 and H_2O. In addition, the α-MnO_2@Co_3O_4 catalyst also exhibited excellent stability and water resistance during the toluene oxidation.[120] Zhang et al.[155] found that the fluorine (F)-doped titanium dioxide (TiO_2) coupled with a small number of α-MnO_2 nanowires could effectively improve the photocatalytic degradation effect of toluene. Specifically, the toluene degradation efficiency before coupling was about 90%, and the toluene degradation efficiency after coupling was increased to 96%.

4.2.3 Phenol. Phenol is deemed as one of the most indispensable organic compounds widely used in various fields. However, it is also an aromatic environment pollutant and widely exits in the industrial wastewater, such as petroleum refinery, wood preservation, and coking.[156] Phenol is a highly toxic substance, which has been listed as one of the most important organic pollutants with carcinogenic, mutagenic, and teratogenic hazards.[157] Although MnO_2-based nanowires have been widely used in environmental catalysis, yet there are few studies investigating the application of MnO_2-based nanowire materials in water treatment. Dong et al.[158] found out that
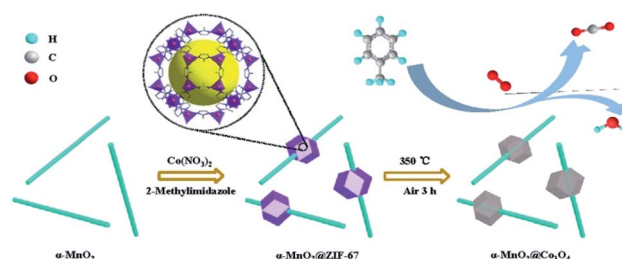

Fig. 14 Proposed mechanism of toluene degradation pathway on α-MnO_2. Reproduced by Huang et al.[87] with permission from Elsevier.

Fig. 15 Illustration of the fabrication of α-MnO_2@Co_3O_4 samples. Reproduced by Ren et al.[120] with permission from Elsevier.

the β-MnO$_2$ nanowires possessed outstanding catalytic performance for phenol degradation. Saputra et al.[159] found that the α-MnO$_2$ materials exhibited different activities in activating peroxymonosulfate to produce sulfate radicals for phenol degradation because of the variety in the phase structure and morphology. The results demonstrated that α-MnO$_2$ nanowire presented the highest activity with stable performance among the investigated nanomaterials. Then, they investigated the effect of phase structure of MnO$_2$-based nanomaterials on the activities in activating oxone to generate sulfate radicals for phenol degradation. As can be seen in Fig. 16, the wire-like α-MnO$_2$ still exhibited higher activity than the rod-like β-MnO$_2$ and fiber-like γ-MnO$_2$ because of the large specific surface area and unique tunnel structure. Besides, the β-MnO$_2$ exhibited the lowest activity due to single tunnel and stable oxygen reducibility. Meanwhile, Peng et al.[160] also illustrated that α-MnO$_2$ nanowires performed higher activity than α-MnO$_2$ nanotubes in the catalytic phenol degradation. The probable reason for this was that α-MnO$_2$ nanowire possessed much greater surface area and lower negative surface charge density than the α-MnO$_2$ nanotube, further accounting for the higher catalytic activities. Liang et al.[161] synthesized the mesoporous Co$_3$O$_4$/α-MnO$_2$ catalyst exhibiting greatly high activity in peroxymonosulfate activation for phenol degradation with 100% conversion in 20 min. The stability tests also showed that the mesoporous Co$_3$O$_4$/MnO$_2$ catalyst presented excellent stability of phenol degradation in several runs without evident deactivation.

4.2.4 Formaldehyde. Formaldehyde (HCHO) has been extensively considered as one of the most harmful indoor VOCs closely related to the human health. As well known, most of the indoor decoration materials will release formaldehyde. Besides, the incomplete combustion of fuel and tobacco will also generate formaldehyde. The formaldehyde is not only a carcinogen but also greatly harmful to the eyes, nose, respiratory system, nervous system, and cardiovascular system.[162–164] Therefore, it is greatly urgent and necessary to effectively reduce the indoor HCHO to improve air quality and reduce public health risks. The catalytic oxidation of HCHO has been considered as a facile, green, and sustainable route. The noble metal catalysts commonly used for HCHO oxidation mainly

contain platinum.[165–167] Therefore, their widely industrial and commercial applications are severely restricted because of the high cost. Sekine et al.[168] found that MnO$_2$ could react with HCHO and release CO$_2$ even at room temperature. This indicated that MnO$_2$ possessed great potential applications as the efficient catalysts in the catalytic oxidation of HCHO and could also be used as catalyst supports. Wang et al.[169] proposed a possible HCHO oxidation mechanism over the partially crystallized mesoporous MnO$_x$ catalyst under dry condition based on the MvK mechanism. As shown in the Fig. 17, firstly, the free oxygen molecules can be captured by oxygen vacancies on the surface of the catalyst. Then, the captured oxygen molecules are stripped and further decomposed into active oxygen species (i.e., adsorbed oxygen: O$_{ads}$); Secondly, Mn^{3+} is oxidized into Mn^{4+} by O$_{ads}$ and meanwhile one electron is released to O$_{ads}$ to produce O$^-$.[170,171] Thirdly, the adsorbed HCHO on the surface of manganese oxide is oxidized into the HCOOH intermediate by the O$^-$. During this process, an electron will transfer from O$^-$ to manganese cations and reduce Mn^{4+} to Mn^{3+} at the same time. Subsequently, the HCOOH intermediate further decomposes into H$^+$ and HCOO$^-$.[168,172] The HCOO$^-$ subsequently reacts with another O$_{ads}$ to produce HCO$_3^-$ and HCO$_3^-$ is finally degraded into H$_2$O and CO$_2$.

Li et al.[174] reported that the sphere-like mesoporous MnO$_2$ exhibited good catalytic activity and reusability for the formaldehyde gas oxidation and the formaldehyde purification efficiency could reach 99% after reacting at room temperature for 2 hours. Zhang et al.[94] studied the catalytic activity of formaldehyde oxidation over the MnO$_2$ nanomaterials with different phase structures (α-, β-, γ- and δ-). It was found that the δ-MnO$_2$ catalyst performed the best activity among these catalysts and could achieve the complete conversion of the HCHO at 80 °C, which was much lower than the α, β, and γ-MnO$_2$ at 125 °C, 200 °C, 150 °C, respectively. Besides, previous researches revealed that the Au-doped[175] and Ag-loading[176] α-MnO$_2$ nanorods exhibited superior catalytic performances of HCHO oxidation. The 100% conversion of HCHO could be achieved at 75 °C and 80 °C over the Au-doped and Ag-loading α-MnO$_2$ nanorods, respectively. Rong et al.[86] prepared (310) facet
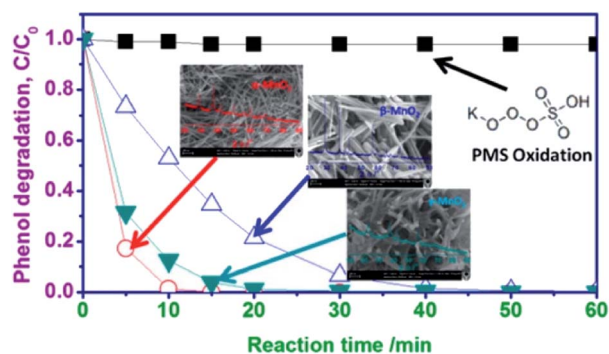

Fig. 16 Phenol degradation of MnO$_2$-based nanomaterials with different phase structures. Reproduced by Saputra et al.[29] with permission from ACS.
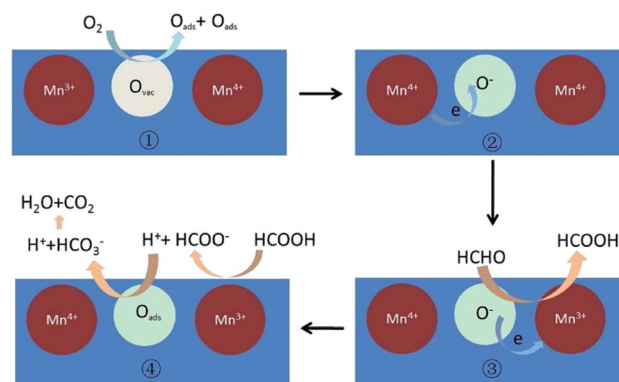

Fig. 17 The possible mechanism of catalytic oxidation of HCHO to CO$_2$ on partially crystallized mesoporous MnO$_x$ under dry condition. Reproduced by Guan et al.[173] with permission from Elsevier.

exposed α-MnO$_2$ nanowire catalyst through crystal facet engineering with superior HCHO oxidation activity. It could completely convert HCHO into CO$_2$ at 60 °C and achieve 86% conversion rate of 0.53 mg m^{-3} HCHO at room temperature. He et al.[177] enhanced the catalytic oxidation of HCHO at ambient temperature over the α-MnO$_2$ with four well-defined morphologies (nanowire, nanotube, nanorod, and nanoflower) with the help of the mechanical vibration. Among them, α-MnO$_2$ nanowires exhibited the best catalytic activity with 100% conversion of 125 ppm HCHO at ambient temperature owing to the high oxygen vacancy concentration.

4.2.5 Methyl mercaptan. Methyl mercaptan (CH$_3$SH) is a highly toxic and corrosive sulfur-containing VOC (S-VOCs). It is widely released from sewage treatment and sanitary landfill.[178] The exposure of CH$_3$SH at few ppm-level can make the human feel unpleasant and dozens of ppm-level can cause significant poisoning.[179,180] In these years, the catalytic removal of CH$_3$SH has been extensively studied. Catalytic combustion technology is considered as one of the most efficient technologies to convert S-VOCs into less toxic products (CO$_2$, SO$_4^{2-}$, etc). But the temperature of catalytic combustion technology is usually higher than 300 °C, which consumes high energy and leads to the sintering of catalysts.[181–185] Currently, catalytic ozonation has been recognized as a promising approach owing to its advantages of high efficiency and complete oxidation of S-VOCs under mild conditions.[186,187] In most studies, supported noble metals (Au, Ag, Pt and Pd, etc.) and low-cost metal oxides like NiO, Fe$_2$O$_3$/Fe$_3$O$_4$, MnO$_x$, and Co$_3$O$_4$ have been developed as efficient catalysts for the catalytic ozonation of S-VOCs.[187] MnO$_2$ is the most widely studied due to its plentiful valence states, versatile structures, high stability, and low cost.

The oxygen vacancies in MnO$_2$ are usually considered as the active sites for O$_3$ adsorption and catalysing ozonation.[188] Fig. 18 shows the adsorption of CH$_3$SH over the MnO$_2$ catalyst and the mechanism of catalytic ozone.[93] O$_3$ can be captured and decomposed by the structural defects on the MnO$_2$ surface, then transformed into activate oxygen species (O^{2-}/O$_2^{2-}$), and quickly evolved into ·O$_2^-$/·OH/^{1}O$_2$ through a chain cycle reaction, which can directly participate in CH$_3$SH and adsorbed CH$_3$S$^-$ oxidation. It is desirable to obtain highly active crystal facets with abundant oxygen vacancies through surface engineering to improve the catalytic activity. He et al.[93] prepared α-MnO$_2$ nanowire with different crystal facets exposed and successfully employed them to catalyse the ozonation of CH$_3$SH. The synthesized 310-MnO$_2$ catalyst performed higher activity than the 110-MnO$_2$ and 100-MnO$_2$. In addition, previous researches found that loading the metal active sites on MnO$_2$ nanomaterials could also enhance the ozonation catalysis of CH$_3$SH.[187,189] Xia et al.[187] prepared Ag deposited three-dimensional MnO$_2$ porous hollow microspheres (Ag/MnO$_2$ PHMSs). The optimal 0.3% Ag/MnO$_2$ PHMSs could completely degrade 70 ppm CH$_3$SH within 600 seconds, displaying much higher efficiency than that of the pristine MnO$_2$ PHMSs support (79%). Additionally, the catalyst retained long-term stability and could be facilely regenerated to its initial activity with ethanol and HCl. Yang et al.[189] synthesized urchin-like oxygen vacancy-rich (V$_O$) hollow-structured MnO$_2$ with the loading of CuO
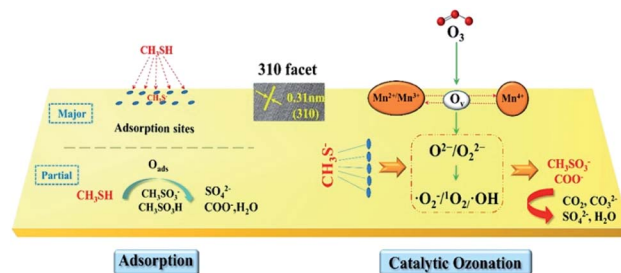

Fig. 18 Mechanism of adsorption and catalytic ozonation toward CH$_3$SH by 310-α-MnO$_2$ catalysts. Reproduced by He et al.[93] with permission from ACS.

nanoparticles on the surface (CuO/V$_O$-MnO$_2$). The well-dispersed CuO on the surface of urchin-like hollow MnO$_2$ enhanced the chemisorption of CH$_3$SH, thus promoting the efficient decomposition of CH$_3$SH on the CuO/V$_O$-MnO$_2$. Among the as-prepared CuO/V$_O$-MnO$_2$ catalyst, the 5CuO/V$_O$-MnO$_2$ realized the optimum CH$_3$SH removal efficiency (98.5%) within 1200 s reaction under 25 °C, which was obviously higher than that of individual MnO$_2$ (70.7%) and CuO (57.0%).

However, there are few researches about the wire-like MnO$_2$ for the ozonation of CH$_3$SH except for the study of He.[93] In view of the strong interaction between wire-like MnO$_2$ and noble/transition metals, more attentions will be attributed to the metal loading/doping of MnO$_2$ nanowire for the ozonation of CH$_3$SH in the future research.

4.3 Ozone

Ozone (O$_3$) is a light blue gas with special odor and strong oxidizing ability. O$_3$ usually can accomplish the complete oxidation of VOCs at room temperature. Therefore, the ozone is widely used as the oxidant in environmental treatment. However, when the amount of the pollutants, such as VOCs, are very large, the balance of ozone in the atmosphere will be broken, leading to the ozone pollution. Besides, the exposure to low-level ozone usually can cause serious effects on the human body's heart, lungs, respiratory tract, and cardiovascular system.[190–193] The catalysts used for the degradation of ozone can be divided into noble metals,[194,195] transition metal oxides[196–201] and noble transition compounds.[202] In the view of the cost and large-scale application, the studies on the catalytic decomposition of ozone have been mainly focused on transition metal oxides, especially MnO$_2$.

α-MnO$_2$ is a newly emerging material for catalytic decomposition of ozone. Jia et al.[141] investigated the ozone removal activity over the MnO$_2$ with different phase structures (α, β, and γ). They found that α-MnO$_2$ performed the highest ozone removal efficiency. Zhu et al.[203] developed a hierarchical structure consisted of graphene encapsulating α-MnO$_2$ nanofiber to address the challenges of the low stability and water inactivation during ozone decomposition. The optimized catalyst exhibited high ozone conversion efficiency of 80% and excellent stability over 100 h under a relative humidity (RH) of 20%. Even though the RH was as high as 50%, the ozone conversion also
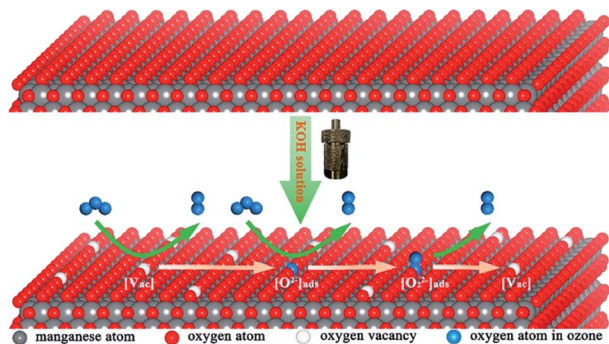
Fig. 19 Schematic of ozone catalytic decomposition on the K-rich MnO$_2$. Reproduced by Zhu et al.[82] with permission from ACS.

could reach 70%, well beyond the performance of α-MnO$_2$ nanofiber. Zhang et al.[155] found that introducing α-MnO$_2$ nanowires into the fluorine (F)-doped titanium dioxide (TiO$_2$) could not only improve the photocatalytic degradation of toluene but also remove almost the total O$_3$ in the system. As the comparison, only 15.8% of O$_3$ could be removed by the pristine F–TiO$_2$ catalyst without mixing with α-MnO$_2$. This indicated that α-MnO$_2$ nanowire was an excellent catalyst for O$_3$ decomposition. Previous study showed that the oxygen vacancies on MnO$_2$ nanomaterials were active sites for ozone adsorption and further decomposition,[199] which largely determined the catalytic degradation activity of MnO$_2$. Zhu et al.[82] developed the α-MnO$_2$ nanowire with high K$^+$ content in tunnel structure through the simple KOH solution post-treatment. As shown in Fig. 19, the substantial increase in K$^+$ content reduced the formation energy of oxygen vacancies, which was further conducive to the formation of oxygen vacancies in the crystal lattice. As a result, the ozone removal performance was improved by doping K$^+$. However, peroxide species (O$_2^{2-}$) could accumulate on the surface of the catalyst and further evolve into relatively stable oxygen, resulting in the decrease in the ozone removal rate. Therefore, the accumulation of intermediate oxygen was a key factor limiting the high efficiency and sustainability of ozone decomposition. Liu et al.[204] prepared cerium-modified todorokite-type manganese dioxides (Ce–MnO$_2$). The as-obtained catalyst showed greatly improved stability, which could keep $\sim$98% of removal efficiency for $\sim$115 ppm of O$_3$ within 5 h under a very high space velocity of 1200 L g^{-1} h^{-1} at room temperature. Besides, the Ce–MnO$_2$ catalyst also exhibited highly stable O$_3$ removal efficiency at temperature as low as 0 °C.

5. Summary and prospect

MnO$_2$-based nanowires are becoming one of the most popular and promising catalysts in environmental applications due to their high catalytic performance, low cost and environmental friendliness. This review systematically summarizes the preparation methods of MnO$_2$-based nanowires, and the effects of phase structure, crystal facet, and morphology on their environmentally catalytic performance. In addition, this review also summarizes their applications in environmental pollution control, such as CO oxidation, removal of VOCs, and the decomposition of O$_3$.

(1) Hydrothermal is a flexible and diverse preparation method, which can facilely control the phase structure, morphology, and exposed crystal facets of the product by changing hydrothermal reaction conditions and has been widely used in laboratory research of MnO$_2$ nanowires. As for the reflux method, it has various advantages (e.g. simple operation procedure, mild reaction condition, and low cost) and is suitable for the large-scale industrial synthesis. However, it is difficult for the sol–gel method alone to obtain wire-like MnO$_2$-based nanomaterials. Therefore, it is often used in combination with template method to prepare highly ordered MnO$_2$ nanowires. However, the employment of the templates will increase the cost of the preparation.

(2) Crystal facet engineering is the research hotspot in the field of MnO$_2$ nanowires. Compared with the influences of phase structure and morphology, it has more significant impact on the catalytic activity of MnO$_2$ nanowires in environmental catalysis.

(3) Doping and/or loading the metals or their oxides can effectively improve the chemical bond strength, phase structure, and electronic structure of the MnO$_2$ nanowires. As a result, the catalytic performance will be improved by increasing the fluidity of oxygen.

Up to now, lots of MnO$_2$-based nanowire material modulation strategies have been developed and their performances in the fields of environmental catalysis have also been promoted. However, the environmental applications of MnO$_2$-based nanowire materials are still at the early stage with various challenges and have a long way to go before the practical applications, specifically in the following aspects.

(1) The complex crystal structures and the morphology diversity of MnO$_2$ result in challenging obstacles in obtaining pure phase structures and uniform morphologies of MnO$_2$ nanowires. Therefore, it is urgent to develop stable and efficient strategies to fabricate MnO$_2$ nanowires in single-crystalline solids with uniform morphology. Considering the remarkable improvement of the catalytic oxidation ability of MnO$_2$ nanowire by the crystal facet engineering, novel synthesis strategies for MnO$_2$ nanowire exposed a high proportion of specific crystal facet should be investigated in depth.

(2) The crystal facet engineering of MnO$_2$ nanowire is mostly focused on the catalysis of VOCs. It can be predicted that it will also have great potential application in catalytic CO oxidation and ozone degradation. However, there are few studies in these areas. Different crystal facets have different catalytic oxidation performances toward specific VOCs. Therefore, it is of great urgency and necessity to systematically investigate the special functions of each crystal facet of MnO$_2$, and finally verify the types of VOCs matched.

(3) Previous studies mainly focused on the noble metals (Au and Ag) and transition metals (Fe, Co, Ni, and Cu) loading or doping. However, few studies have focused on the modification of MnO$_2$ nanowire by loading or doping rare earth metals (La, Ce, Pr, and Sm). In view of the improvement of the O$_3$ removal

efficiency of MnO_2 at low temperature by the cerium doping, the effect of catalytic degradation of other air pollutants by the rare earth metals modification should be explored in the future.

(4) Although MnO_2-based nanowire materials as the supports or the efficient catalysts are gradually emerging in the field of environmental catalysis, yet there is still giant gap between the laboratory results and actually industrial requirement in the aspects of the catalytic performance, long-term stability, and water resistance of removing CO and VOCs at relatively low temperature compared with traditional noble metal catalysts.

Author contributions

LX: conceived ideas, made comments, edited; YX: investigation, writing – original draft; GC, CW, NW: assisted YX in literature research and summary; LX, MC, XH: investigation, supervision, funding acquisition. All authors discussed the results and contributed to the final manuscript.

Conflicts of interest

There are no conflicts to declare.

Acknowledgements

References

1 S. Dey and G. C. Dhal, *Mater. Sci. Energy Technol.*, 2019, **2**, 607–623.

2 M. S. Kamal, S. A. Razzak and M. M. Hossain, *Atmos. Environ.*, 2016, **140**, 117–134.

3 Q. Liu, C. X. Liu, X. L. Nie, L. Bai and S. H. Wen, *Mater. Lett.*, 2012, **72**, 101–103.

4 K. J. Cole, A. F. Carley, M. J. Crudace, M. Clarke, S. H. Taylor and G. J. Hutchings, *Catal. Lett.*, 2010, **138**, 143–147.

5 M. T. Salam, J. Millstein, Y. F. Li, F. W. Lurmann, H. G. Margolis and F. D. Gilliland, *Environ. Health Perspect.*, 2005, **113**, 1638–1644.

6 M. Wilhelm and B. Ritz, *Environ. Health Perspect.*, 2005, **113**, 1212–1221.

7 K. Guo, W. W. Kong and Z. M. Yang, *Plant, Cell Environ.*, 2009, **32**, 1033–1045.

8 K. Guo, K. Xia and Z. M. Yang, *J. Exp. Bot.*, 2008, **59**, 3443–3452.

9 Z. Hu, Y. Utiskul, J. G. Quintiere and A. Trouve, *Proc. Combust. Inst.*, 2007, **31**, 2537–2545.

10 P. Fagone, K. Mangano, S. Mammana, E. Cavalli, R. Di Marco, M. L. Barcellona, L. Salvatorelli, G. Magro and F. Nicoletti, *Clin. Immunol.*, 2015, **157**, 198–204.

11 R. N. Colvile, E. J. Hutchinson, J. S. Mindell and R. F. Warren, *Atmos. Environ.*, 2001, **35**, 1537–1565.

12 Y. C. Yao, J. H. Tsai, H. F. Ye and H. L. Chiang, *J. Air Waste Manage. Assoc.*, 2009, **59**, 1339–1346.

13 M. M. Schubert, S. Hackenberg, A. C. van Veen, M. Muhler, V. Plzak and R. J. Behm, *J. Catal.*, 2001, **197**, 113–122.

14 B. K. Min and C. M. Friend, *Chem. Rev.*, 2007, **107**, 2709–2724.

15 B. T. Qiao, A. Q. Wang, X. F. Yang, L. F. Allard, Z. Jiang, Y. T. Cui, J. Y. Liu, J. Li and T. Zhang, *Nat. Chem.*, 2011, **3**, 634–641.

16 G. X. Chen, Y. Zhao, G. Fu, P. N. Duchesne, L. Gu, Y. P. Zheng, X. F. Weng, M. S. Chen, P. Zhang, C. W. Pao, J. F. Lee and N. F. Zheng, *Science*, 2014, **344**, 495–499.

17 K. Liu, A. Q. Wang and T. Zhang, *ACS Catal.*, 2012, **2**, 1165–1178.

18 L. Y. Zhang, H. Y. Liu, X. Huang, X. P. Sun, Z. Jiang, R. Schlogl and D. S. Su, *Angew. Chem., Int. Ed.*, 2015, **54**, 15823–15826.

19 T. Bunluesin, H. Cordatos and R. J. Gorte, *J. Catal.*, 1995, **157**, 222–226.

20 X. W. Xie, Y. Li, Z. Q. Liu, M. Haruta and W. J. Shen, *Nature*, 2009, **458**, 746–749.

21 D. Gu, C. J. Jia, C. Weidenthaler, H. J. Bongard, B. Spliethoff, W. Schmidt and F. Schuth, *J. Am. Chem. Soc.*, 2015, **137**, 11407–11418.

22 M. Y. Guo, F. Z. Liu, J. Tsui, A. A. Voskanyan, A. M. C. Ng, A. B. Djurisic, W. K. Chan, K. Y. Chan, C. Z. Liao, K. M. Shih and C. Surya, *J. Mater. Chem. A*, 2015, **3**, 3627–3632.

23 S. Royer and D. Duprez, *Chemcatchem*, 2011, **3**, 24–65.

24 Y. Ren, Z. Ma, L. P. Qian, S. Dai, H. Y. He and P. G. Bruce, *Catal. Lett.*, 2009, **131**, 146–154.

25 K. Ramesh, L. W. Chen, F. X. Chen, Y. Liu, Z. Wang and Y. F. Han, *Catal. Today*, 2008, **131**, 477–482.

26 S. H. Liang, F. T. G. Bulgan, R. L. Zong and Y. F. Zhu, *J. Phys. Chem. C*, 2008, **112**, 5307–5315.

27 B. B. He, G. Cheng, S. F. Zhao, X. H. Zeng, Y. F. Li, R. N. Yang, M. Sun and L. Yu, *J. Solid State Chem.*, 2019, **269**, 305–311.

28 T. Wang, S. Chen, H. G. Wang, Z. Liu and Z. B. Wu, *Chin. J. Catal.*, 2017, **38**, 793–804.

29 E. Saputra, S. Muhammad, H. Q. Sun, H. M. Ang, M. O. Tade and S. B. Wang, *Environ. Sci. Technol.*, 2013, **47**, 5882–5887.

30 J. Li, Z. Qu, Y. Qin and H. Wang, *Appl. Surf. Sci.*, 2016, **385**, 234–240.

31 W. X. Tang, M. S. Yao, Y. Z. Deng, X. F. Li, N. Han, X. F. Wu and Y. F. Chen, *Chem. Eng. J.*, 2016, **306**, 709–718.

32 S. Zhu, S. H. Ho, C. Jin, X. Duan and S. Wang, *Environ. Sci.: Nano*, 2020, **7**, 368–396.

33 L. Miao, J. L. Wang and P. Y. Zhang, *Appl. Surf. Sci.*, 2019, **466**, 441–453.

34 J. Chen, H. M. Meng, Y. Tian, R. Yang, D. Du, Z. H. Li, L. B. Qu and Y. H. Lin, *Nanoscale Horiz.*, 2019, **4**, 321–338.

35 B. B. Ding, P. Zheng, P. A. Ma and J. Lin, *Adv. Mater.*, 2020, **32**, 1905823.

36 W. Li, K. Xu, L. An, F. Jiang, X. Zhou, J. Yang, Z. Chen, R. Zou and J. Hu, *J. Mater. Chem. A*, 2014, **2**, 1443–1447.

37 W. Li, Q. Liu, Y. Sun, J. Sun, R. Zou, G. Li, X. Hu, G. Song, G. Ma, J. Yang, Z. Chen and J. Hu, *J. Mater. Chem.*, 2012, **22**, 14864–14867.

38 J. Li, W. Li, L. Huang, C. Ma and T. Ji, *J. Nanoelectron. Optoelectron.*, 2021, **16**, 149–156.

39 R. A. Davoglio, G. Cabello, J. F. Marco and S. R. Biaggio, *Electrochim. Acta*, 2018, **261**, 428–435.

40 J. G. Wang, F. Y. Kang and B. Q. Wei, *Prog. Mater. Sci.*, 2015, **74**, 51–124.

41 W. Guo, C. Yu, S. F. Li, Z. Wang, J. H. Yu, H. W. Huang and J. S. Qiu, *Nano Energy*, 2019, **57**, 459–472.

42 X. Guo, S. Yang, D. Wang, A. Chen, Y. Wang, P. Li, G. Liang and C. Zhi, *Curr. Opin. Electrochem.*, 2021, **30**, 100769.

43 A. K. Worku, D. W. Ayele, N. G. Habtu, M. A. Teshager and Z. G. Workineh, *Materials Today Sustainability*, 2021, **13**, 100072.

44 R. J. Yang, Y. Y. Fan, R. Q. Ye, Y. X. Tang, X. H. Cao, Z. Y. Yin and Z. Y. Zeng, *Adv. Mater.*, 2021, **33**, 2004862.

45 Y. Long, J. F. Hui, P. P. Wang, S. Hu, B. Xu, G. L. Xiang, J. Zhuang, X. Q. Lv and X. Wang, *Chem. Commun.*, 2012, **48**, 5925–5927.

46 D. Portehault, S. Cassaignon, E. Baudrin and J. P. Jolivet, *Chem. Mater.*, 2008, **20**, 6140–6147.

47 R. R. Jiang, T. Huang, J. L. Liu, J. H. Zhuang and A. S. Yu, *Electrochim. Acta*, 2009, **54**, 3047–3052.

48 J. C. Villegas, L. J. Garces, S. Gomez, J. P. Durand and S. L. Suib, *Chem. Mater.*, 2005, **17**, 1910–1918.

49 M. S. Wu, J. T. Lee, Y. Y. Wang and C. C. Wan, *J. Phys. Chem. B*, 2004, **108**, 16331–16333.

50 R. N. DeGuzman, Y. F. Shen, E. J. Neth, S. L. Suib, C. L. O'Young, S. Levine and J. M. Newsam, *Chem. Mater.*, 1994, **6**, 815–821.

51 X. Wang and Y. D. Li, *Chem. –Eur. J.*, 2003, **9**, 300–306.

52 M. Wei, Y. Konishi, H. Zhou, H. Sugihara and H. Arakawa, *Nanotechnology*, 2005, **16**, 245–249.

53 X. Zhang, W. Yang, J. Yang and D. G. Evans, *J. Cryst. Growth*, 2008, **310**, 716–722.

54 X. Y. Wang, X. Y. Wang, W. G. Huang, P. J. Sebastian and S. Gamboa, *J. Power Sources*, 2005, **140**, 211–215.

55 W. X. Tang, X. Shan, S. D. Li, H. D. Liu, X. F. Wu and Y. F. Chen, *Mater. Lett.*, 2014, **132**, 317–321.

56 D. Gu, J. C. Tseng, C. Weidenthaler, H. J. Bongard, B. Spliethoff, W. Schmidt, F. Soulimani, B. M. Weckhuysen and F. Schuth, *J. Am. Chem. Soc.*, 2016, **138**, 9572–9580.

57 D. Zitoun, N. Pinna, N. Frolet and C. Belin, *J. Am. Chem. Soc.*, 2005, **127**, 15034–15035.

58 X. H. Su, L. Yu, G. Cheng, H. H. Zhang, M. Sun and X. F. Zhang, *Appl. Energy*, 2015, **153**, 94–100.

59 D. J. Davis, T. N. Lambert, J. A. Vigil, M. A. Rodriguez, M. T. Brumbach, E. N. Coker and S. J. Limmer, *J. Phys. Chem. C*, 2014, **118**, 17342–17350.

60 T. N. Lambert, J. A. Vigil, S. E. White, C. J. Delker, D. J. Davis, M. Kelly, M. T. Brumbach, M. A. Rodriguez and B. S. Swartzentruber, *J. Phys. Chem. C*, 2017, **121**, 2789–2797.

61 J. J. Gao, C. M. Jia, L. P. Zhang, H. M. Wang, Y. H. Yang, S. F. Hung, Y. Y. Hsu and B. Liu, *J. Catal.*, 2016, **341**, 82–90.

62 D. Jampaiah, V. K. Velisoju, P. Venkataswamy, V. E. Coyle, A. Nafady, B. M. Reddy and S. K. Bhargava, *ACS Appl. Mater. Interfaces*, 2017, **9**, 32652–32666.

63 W. Wang, Y. Shi, Y. Su, Y. Wang and H. Sun, *Research and Application of Materials Science*, 2019, **1**, 18–23.

64 Y. F. Shen, S. L. Suib and C. L. O'Young, *J. Am. Chem. Soc.*, 1994, **116**, 11020–11029.

65 A. K. Sinha, M. Pradhan and T. Pal, *J. Phys. Chem. C*, 2013, **117**, 23976–23986.

66 N. Kijima, Y. Sakata, Y. Takahashi, J. Akimoto, T. Kumagai, K. Igarashi and T. Shimizu, *Solid State Ionics*, 2009, **180**, 616–620.

67 X. Chen, Y. F. Shen, S. L. Suib and C. L. O'Young, *Chem. Mater.*, 2002, **14**, 940–948.

68 L. Jin, C. H. Chen, V. M. B. Crisostomo, L. P. Xu, Y. C. Son and S. L. Suib, *Appl. Catal., A*, 2009, **355**, 169–175.

69 Y. A. May, S. Wei, W. Z. Yu, W. W. Wang and C. J. Jia, *Langmuir*, 2020, **36**, 11196–11206.

70 T. Uematsu, Y. Miyamoto, Y. Ogasawara, K. Suzuki, K. Yamaguchi and N. Mizuno, *Catal. Sci. Technol.*, 2016, **6**, 222–233.

71 F. Hashemzadeh, M. M. K. Motlagh and A. Maghsoudipour, *J. Sol-Gel Sci. Technol.*, 2009, **51**, 169–174.

72 S. Ching, E. J. Welch, S. M. Hughes, A. B. F. Bahadoor and S. L. Suib, *Chem. Mater.*, 2002, **14**, 1292–1299.

73 S. Ching, D. J. Petrovay, M. L. Jorgensen and S. L. Suib, *Inorg. Chem.*, 1997, **36**, 883–890.

74 E. Hastuti, W. R. Agustin and I. Yuliana, *IOP Conf. Ser., Earth Environ. Sci.*, 2020, **456**, 012017.

75 S. Ching, J. L. Roark, N. Duan and S. L. Suib, *Chem. Mater.*, 1997, **9**, 750–754.

76 A. M. Hashem, A. E. Abdel-Ghany, R. El-Tawil, A. Bhaskar, B. Hunzinger, H. Ehrenberg, A. Mauger and C. M. Julien, *Ionics*, 2016, **22**, 2263–2271.

77 M. H. Ghorbani and A. M. Davarpanah, *Mod. Phys. Lett. B*, 2017, **31**, 1750006.

78 S. F. Chin, S. C. Pang and M. A. Anderson, *Mater. Lett.*, 2010, **64**, 2670–2672.

79 L. F. Liu, H. W. Zhang, Y. S. Zhang, D. M. Cao and X. H. Zhao, *Colloids Surf., A*, 2015, **468**, 280–284.

80 J. L. Zhang, T. Zhuang, S. J. Liu, G. C. Zhang and K. L. Huo, *J. Environ. Chem. Eng.*, 2020, **8**, 103967.

81 H. Q. Wang, M. B. Zheng, J. H. Chen, G. B. Ji and J. M. Cao, *J. Nanotechnol.*, 2010, **2010**, 479172.

82 G. X. Zhu, J. G. Zhu, W. L. Li, W. Q. Yao, R. L. Zong, Y. F. Zhu and Q. F. Zhang, *Environ. Sci. Technol.*, 2018, **52**, 8684–8692.

83 G. Cheng, L. Yu, B. Lan, M. Sun, T. Lin, Z. W. Fu, X. H. Su, M. Q. Qiu, C. H. Guo and B. Xu, *Mater. Res. Bull.*, 2016, **75**, 17–24.

84 M. Sadeghinia, M. Rezaei and E. Amini, *Korean J. Chem. Eng.*, 2013, **30**, 2012–2016.

85 Z. Wu, J. Wu, X. Sun, B. Liu and J. Shen, *Sci. Sin.: Chim.*, 2017, **47**, 1226–1232.

86 S. P. Rong, P. Y. Zhang, F. Liu and Y. J. Yang, *ACS Catal.*, 2018, **8**, 3435–3446.

87 J. Huang, R. M. Fang, Y. J. Sun, J. Y. Li and F. Dong, *Chemosphere*, 2021, **263**, 128103.

88 X. Wang and Y. D. Li, *J. Am. Chem. Soc.*, 2002, **124**, 2880–2881.

89 V. Subramanian, H. W. Zhu, R. Vajtai, P. M. Ajayan and B. Q. Wei, *J. Phys. Chem. B*, 2005, **109**, 20207–20214.

90 D. S. Zheng, S. X. Sun, W. L. Fan, H. Y. Yu, C. H. Fan, G. X. Cao, Z. L. Yin and X. Y. Song, *J. Phys. Chem. B*, 2005, **109**, 16439–16443.

91 K. Li, C. Chen, H. B. Zhang, X. J. Hu, T. H. Sun and J. P. Jia, *Appl. Surf. Sci.*, 2019, **496**, 143662.

92 K. Z. Li, J. J. Chen, V. Peng, W. C. Lin, T. Yan and J. H. Li, *J. Mater. Chem. A*, 2017, **5**, 20911–20921.

93 C. He, Y. C. Wang, Z. Y. Li, Y. J. Huang, Y. H. Liao, D. H. Xia and S. C. Lee, *Environ. Sci. Technol.*, 2020, **54**, 12771–12783.

94 J. H. Zhang, Y. B. Li, L. Wang, C. B. Zhang and H. He, *Catal. Sci. Technol.*, 2015, **5**, 2305–2313.

95 X. G. Han, Q. Kuang, M. S. Jin, Z. X. Xie and L. S. Zheng, *J. Am. Chem. Soc.*, 2009, **131**, 3152–3153.

96 J. S. Chen, T. Zhu, X. H. Yang, H. G. Yang and X. W. Lou, *J. Am. Chem. Soc.*, 2010, **132**, 13162–13164.

97 T. Kropp, J. Paier and J. Sauer, *J. Phys. Chem. C*, 2017, **121**, 21571–21578.

98 G. Liu, J. C. Yu, G. Q. Lu and H. M. Cheng, *Chem. Commun.*, 2011, **47**, 12889.

99 B. Y. Bai and J. H. Li, *ACS Catal.*, 2014, **4**, 2753–2762.

100 X. F. Tang, J. L. Chen, Y. G. Li, Y. Li, Y. D. Xu and W. J. Shen, *Chem. Eng. J.*, 2006, **118**, 119–125.

101 F. Wang, H. X. Dai, J. G. Deng, G. M. Bai, K. M. Ji and Y. X. Liu, *Environ. Sci. Technol.*, 2012, **46**, 4034–4041.

102 F. J. Shi, F. Wang, H. X. Dai, J. X. Dai, J. G. Deng, Y. X. Liu, G. M. Bai, K. M. Ji and C. T. Au, *Appl. Catal., A*, 2012, **433**, 206–213.

103 J. C. Liu, O. Margeat, W. Dachraoui, X. J. Liu, M. Fahlman and J. Ackermann, *Adv. Funct. Mater.*, 2014, **24**, 6029–6037.

104 H. X. Tang, Z. Zhou and H. A. Sodano, *ACS Appl. Mater. Interfaces*, 2014, **6**, 5450–5455.

105 X. H. Liao, Y. Jiang, G. K. Jian, G. Cheng and M. Sun, *J. Guangdong Univ. Technol.*, 2018, **35**, 75–79.

106 M. Wojciechowska, A. Malczewska, B. Czajka, M. Zieliński and J. Goslar, *Appl. Catal., A*, 2002, **237**, 63–70.

107 E. W. McFarland and H. Metiu, *Chem. Rev.*, 2013, **113**, 4391–4427.

108 L. C. Wang, X. S. Huang, Q. Liu, Y. M. Liu and J. H. Zhuang, *J. Catal.*, 2008, **259**, 66–74.

109 Y. Qin, Y. Wang, J. M. Li and Z. P. Qu, *Surf. Interfaces*, 2020, **21**, 100657.

110 T. N. Lambert, D. J. Davis, W. Lu, S. J. Limmer, P. G. Kotula, A. Thuli, M. Hungate, G. D. Ruan, Z. Jin and J. M. Tour, *Chem. Commun.*, 2012, **48**, 7931–7933.

111 M. J. Zhou, L. L. Cai, M. Bajdich, M. Garcia-Melchor, H. Li, J. J. He, J. Wilcox, W. D. Wu, A. Vojvodic and X. L. Zheng, *ACS Catal.*, 2015, **5**, 4485–4491.

112 J. S. Elias, M. Risch, L. Giordano, A. N. Mansour and Y. Shao-Horn, *J. Am. Chem. Soc.*, 2014, **136**, 17193–17200.

113 W. Liu and M. Flytzani-Stephanopoulos, *Chem. Eng. J. Biochem. Eng. J.*, 1996, **64**, 283–294.

114 Z. Boukha, J. L. Ayastuy, A. Iglesias-Gonzalez, B. Pereda-Ayo, M. A. Gutierrez-Ortiz and J. R. Gonzalez-Velasco, *Appl. Catal., B*, 2014, **160**, 629–640.

115 H. L. Jiang and Q. Xu, *J. Mater. Chem.*, 2011, **21**, 13705–13725.

116 M. Han, S. L. Liu, L. Y. Zhang, C. Zhang, W. W. Tu, Z. H. Dai and J. C. Bao, *ACS Appl. Mater. Interfaces*, 2012, **4**, 6654–6660.

117 Z. C. Wu, Y. J. Xue, H. Wang, Y. Q. Wu and H. Yu, *RSC Adv.*, 2014, **4**, 59009–59016.

118 S. S. Li, J. N. Zheng, A. J. Wang, F. L. Tao, J. J. Feng, J. R. Chen and H. Y. Yu, *J. Power Sources*, 2014, **272**, 1078–1085.

119 X. W. Teng, W. Q. Han, Q. Wang, L. Li, A. I. Frenkel and J. C. Yang, *J. Phys. Chem. C*, 2008, **112**, 14696–14701.

120 Q. M. Ren, S. P. Mo, J. Fan, Z. T. Feng, M. Y. Zhang, P. R. Chen, J. J. Gao, M. L. Fu, L. M. Chen, J. L. Wu and D. Q. Ye, *Chin. J. Catal.*, 2020, **41**, 1873–1883.

121 Y. Z. Deng, W. X. Tang, W. H. Li and Y. F. Chen, *Catal. Today*, 2018, **308**, 58–63.

122 J. P. Ma, Q. Y. Zhao, D. L. Wei, H. Q. Liu, X. K. Wang, Z. Chen and J. J. Wang, *Inorg. Chem. Front.*, 2019, **6**, 1011–1021.

123 J. Zhou, L. F. Qin, W. Xiao, C. Zeng, N. Li, T. Lv and H. Zhu, *Appl. Catal., B*, 2017, **207**, 233–243.

124 N. Huang, Z. P. Qu, C. Dong, Y. Qin and X. X. Duan, *Appl. Catal., A*, 2018, **560**, 195–205.

125 A. Katsnelson, *C&EN Global Enterprise*, 2019, **97**, 18–21.

126 F. X. Tian, M. Zhu, X. Liu, W. Tu and Y. F. Han, *J. Catal.*, 2021, **401**, 115–128.

127 R. Xu, X. Wang, D. S. Wang, K. B. Zhou and Y. D. Li, *J. Catal.*, 2006, **237**, 426–430.

128 P. P. Wang, J. H. Duan, J. Wang, F. M. Mei and P. Liu, *Chin. J. Catal.*, 2020, **41**, 1298–1310.

129 WHO, *Iarc Monographs on the Evaluation of Carcinogenic Risks to Humans*, Household Use of Solid Fuels and High-Temperature Frying, 2010, vol. 95, pp. 9–38.

130 Y. Dumanoglu, M. Kara, H. Altiok, M. Odabasi, T. Elbir and A. Bayram, *Atmos. Environ.*, 2014, **98**, 168–178.

131 H. Guo, S. C. Lee, P. K. K. Louie and K. F. Ho, *Chemosphere*, 2004, **57**, 1363–1372.

132 A. Srivastava, A. E. Joseph, S. Patil, A. More, R. C. Dixit and M. Prakash, *Atmos. Environ.*, 2005, **39**, 59–71.

133 Y. L. Wang, Z. H. Li, C. Tang, H. X. Ren, Q. Zhang, M. Xue, J. Xiong, D. B. Wang, Q. Yu, Z. Y. He, F. Wei and J. K. Jiang, *Environ. Sci.: Nano*, 2019, **6**, 3113–3122.

134 S. M. Saqer, D. I. Kondarides and X. E. Verykios, *Appl. Catal., B*, 2011, **103**, 275–286.

135 Z. Sihaib, F. Puleo, J. M. Garcia-Vargas, L. Retailleau, C. Descorme, L. F. Liotta, J. L. Valverde, S. Gil and A. Giroir-Fendler, *Appl. Catal., B*, 2017, **209**, 689–700.

136 Y. X. Zeng, Y. J. Zhan, R. J. Xie, K. Hu, J. P. Cao, D. X. Lei, B. Y. Liu, M. He and H. B. Huang, *Chemosphere*, 2020, **244**, 125567.

137 S. Weon, F. He and W. Choi, *Environ. Sci.: Nano*, 2019, **6**, 3185–3214.

138 Y. X. Ruan, H. Guo, J. Li, Z. Y. Liu, N. Jiang and Y. Wu, *Chemosphere*, 2020, **258**, 127334.

139 S. Malakar, P. D. Saha, D. Baskaran and R. Rajamanickam, *Environ. Technol. Innovation*, 2017, **8**, 441–461.

140 S. C. Kim and W. G. Shim, *Appl. Catal., B*, 2010, **98**, 180–185.

141 J. B. Jia, P. Y. Zhang and L. Chen, *Appl. Catal., B*, 2016, **189**, 210–218.

142 H. S. Kim, T. W. Kim, H. L. Koh, S. H. Lee and B. R. Min, *Appl. Catal., A*, 2005, **280**, 125–131.

143 S. F. Zuo, Y. J. Du, F. J. Liu, D. Han and C. Z. Qi, *Appl. Catal., A*, 2013, **451**, 65–70.

144 X. Jiang, J. F. Hua, H. Deng and Z. B. Wu, *J. Mol. Catal. A: Chem.*, 2014, **383**, 188–193.

145 H. H. Kim, S. M. Oh, A. Ogata and S. Futamura, *Catal. Lett.*, 2004, **96**, 189–194.

146 Z. Hu, R. L. Mi, X. Yong, S. Liu, D. Li, Y. Li and T. Zhang, *Chemistryselect*, 2019, **4**, 473–480.

147 Y. Liu, W. J. Zong, H. Zhou, D. S. Wang, R. R. Cao, J. J. Zhan, L. F. Liu and B. W. L. Jang, *Catal. Sci. Technol.*, 2018, **8**, 5344–5358.

148 J. Ma, J. Wang and Y. Dang, *Chem. Eng. J.*, 2020, **388**, 124387.

149 Q. Ye, J. S. Zhao, F. F. Huo, J. Wang, S. Y. Cheng, T. F. Kang and H. X. Dai, *Catal. Today*, 2011, **175**, 603–609.

150 Z. T. Feng, Q. M. Ren, R. S. Peng, S. P. Mo, M. Y. Zhang, M. L. Fu, L. M. Chen and D. Q. Ye, *Catal. Today*, 2019, **332**, 177–182.

151 S. Ren, W. J. Liang, Q. L. Li and Y. X. Zhu, *Chemosphere*, 2020, **251**, 126382.

152 W. H. Yang, Z. A. Su, Z. H. Xu, W. N. Yang, Y. Peng and J. H. Li, *Appl. Catal., B*, 2020, **260**, 118150.

153 C. Dong, H. Wang, Y. W. Ren and Z. P. Qu, *J. Environ. Sci.*, 2021, **104**, 102–112.

154 X. Min, M. M. Guo, L. Z. Liu, L. Li, J. N. Gu, J. X. Liang, C. Chen, K. Li, J. P. Jia and T. H. Sun, *J. Hazard. Mater.*, 2021, **406**, 124743.

155 Y. Zhang, M. Wu, Y. Wang, H. K. Yu and D. Leung, *Appl. Catal., B*, 2021, **280**, 119388.

156 P. K. Arora and H. Bae, *J. Environ. Sci.*, 2014, **13**, 31.

157 A. Kumar, S. Kumar and S. Kumar, *Biochem. Eng. J.*, 2005, **22**, 151–159.

158 Y. M. Dong, H. X. Yang, K. He, S. Q. Song and A. M. Zhang, *Appl. Catal., B*, 2009, **85**, 155–161.

159 E. Saputra, S. Muhammad, H. Q. Sun, A. Patel, P. Shukla, Z. H. Zhu and S. B. Wang, *Catal. Commun.*, 2012, **26**, 144–148.

160 W. C. Peng, S. B. Wang and X. Y. Li, *Sep. Purif. Technol.*, 2016, **163**, 15–22.

161 H. W. Liang, H. Q. Sun, A. Patel, P. Shukla, Z. H. Zhu and S. B. Wang, *Appl. Catal., B*, 2012, **127**, 330–335.

162 R. Maddalena, M. Russell, D. P. Sullivan and M. G. Apte, *Environ. Sci. Technol.*, 2009, **43**, 5626–5632.

163 J. J. Pei and J. S. S. Zhang, *HVACR Res.*, 2011, **17**, 476–503.

164 J. H. Yang, G. S. Yang and Z. Z. Ye, *Appl. Mech. Mater.*, 2014, **668**, 294–297.

165 C. B. Zhang, H. He and K. Tanaka, *Appl. Catal., B*, 2006, **65**, 37–43.

166 S. S. Kim, K. H. Park and S. C. Hong, *Appl. Catal., A*, 2011, **398**, 96–103.

167 J. X. Peng and S. D. Wang, *Appl. Catal., B*, 2007, **73**, 282–291.

168 Y. Sekine, *Atmos. Environ.*, 2002, **36**, 5543–5547.

169 M. Wang, L. X. Zhang, W. M. Huang, T. P. Xiu, C. G. Zhuang and J. L. Shi, *Chem. Eng. J.*, 2017, **320**, 667–676.

170 P. Liu, H. P. He, G. L. Wei, X. L. Liang, F. H. Qi, F. D. Tan, W. Tan, J. X. Zhu and R. L. Zhu, *Appl. Catal., B*, 2016, **182**, 476–484.

171 J. Wang, B. Z. Yeung, M. J. Cui, C. J. Peer, Z. Lu, W. D. Figg, M. G. Wientjes, S. Woo and J. L. S. Au, *J. Controlled Release*, 2017, **268**, 147–158.

172 J. L. Wang, R. Yunus, J. G. Li, P. L. Li, P. Y. Zhang and J. Kim, *Appl. Surf. Sci.*, 2015, **357**, 787–794.

173 S. N. Guan, W. Z. Li, J. R. Ma, Y. Y. Lei, Y. S. Zhu, Q. F. Huang and X. M. Dou, *J. Ind. Eng. Chem.*, 2018, **66**, 126–140.

174 G. Li, X. Ding, Y. Shen and X. Jing, *Knitting Industries*, 2017, **7**, 39–42.

175 J. Chen, D. X. Yan, Z. Xu, X. Chen, W. J. Xu, H. P. Jia and J. Chen, *Environ. Sci. Technol.*, 2018, **52**, 4728–4737.

176 F. L. Huang, X. Wang, Q. Y. Zhu, K. L. Li, X. F. Zhou, S. H. Lu, Z. Fan, L. L. He, Y. X. Liu and F. J. Pang, *Catal. Surv. Asia*, 2019, **23**, 33–40.

177 T. H. He, D. D. Shao, X. S. Zeng and S. P. Rong, *Chemosphere*, 2020, **261**, 127778.

178 J. Huang, S. Zhong, Y. Dai, C. C. Liu and H. Zhang, *Environ. Sci. Technol.*, 2018, **52**, 11309–11318.

179 J. C. Lu, H. S. Hao, L. M. Zhang, Z. Z. Xu, L. P. Zhong, Y. T. Zhao, D. D. He, J. P. Liu, D. K. Chen, H. P. Pu, S. F. He and Y. M. Luo, *Appl. Catal., B*, 2018, **237**, 185–197.

180 J. R. Kastner, K. C. Das, Q. Buquoi and N. D. Melear, *Environ. Sci. Technol.*, 2003, **37**, 2568–2574.

181 J. L. Yang, Q. Zhang, F. Zhang, D. H. Xia, H. D. Liu, S. H. Tian, L. P. Sun, D. Shu, C. He and S. Runa, *J. Hazard. Mater.*, 2018, **358**, 136–144.

182 S. H. Xie, Y. X. Liu, J. G. Deng, X. T. Zhao, J. Yang, K. F. Zhang, Z. Han, H. Arandiyan and H. X. Dai, *Appl. Catal., B*, 2017, **206**, 221–232.

183 H. B. Huang, Y. Xu, Q. Y. Feng and D. Y. C. Leung, *Catal. Sci. Technol.*, 2015, **5**, 2649–2669.

184 Y. T. Zhao, D. K. Chen, J. P. Liu, D. D. He, X. H. Cao, C. Y. Han, J. C. Lu and Y. M. Luo, *Chem. Eng. J.*, 2020, **389**, 124384.

185 D. D. He, G. P. Wan, H. S. Hao, D. K. Chen, J. C. Lu, L. Zhang, F. Liu, L. P. Zhong, S. F. He and Y. M. Luo, *Chem. Eng. J.*, 2016, **289**, 161–169.

186 T. Nothe, H. Fahlenkamp and C. von Sonntag, *Environ. Sci. Technol.*, 2009, **43**, 5990–5995.

187 D. H. Xia, W. J. Xu, Y. C. Wang, J. L. Yang, Y. J. Huang, L. L. Hu, C. He, D. Shu, D. Y. C. Leung and Z. H. Pang, *Environ. Sci. Technol.*, 2018, **52**, 13399–13409.

188 W. Li and G. V. Gibbs, *J. Am. Chem. Soc.*, 1998, **120**, 9041–9046.

189 J. L. Yang, Y. J. Huang, Y. W. Chen, D. H. Xia, C. Y. Mou, L. L. Hu, J. W. Zeng, C. He, P. K. Wong and H. Y. Zhu, *Nano Today*, 2020, **35**, 100944.

190 H. Y. Li, S. W. Wu, L. Pan, J. H. Xu, J. Shan, X. Yang, W. Dong, F. R. Deng, Y. H. Chen, M. Shima and X. B. Guo, *Environ. Pollut.*, 2018, **232**, 358–366.

191 S. Magzamen, B. F. Moore, M. G. Yost, R. A. Fenske and C. J. Karr, *J. Occup. Environ. Med.*, 2017, **59**, 624–630.

192 J. D. Berman, N. Fann, J. W. Hollingsworth, K. E. Pinkerton, W. N. Rom, A. M. Szema, P. N. Breysse, R. H. White and F. C. Curriero, *Environ. Health Perspect.*, 2012, **120**, 1404–1410.

193 B. Hoffmann, H. Luttmann-Gibson, A. Cohen, A. Zanobetti, C. de Souza, C. Foley, H. H. Suh, B. A. Coull, J. Schwartz, M. Mittleman, P. Stone, E. Horton and D. R. Gold, *Environ. Health Perspect.*, 2012, **120**, 241–246.

194 Z. P. Hao, D. Y. Cheng, Y. Guo and Y. H. Liang, *Appl. Catal., B*, 2001, **33**, 217–222.

195 P. Nikolov, K. Genov, P. Konova, K. Milenova, T. Batakliev, V. Georgiev, N. Kumar, D. K. Sarker, D. Pishev and S. Rakovsky, *J. Hazard. Mater.*, 2010, **184**, 16–19.

196 T. Gopi, G. Swetha, S. C. Shekar, C. Ramakrishna, B. Saini, R. Krishna and P. V. L. Rao, *Catal. Commun.*, 2017, **92**, 51–55.

197 S. Y. Gong, J. Y. Chen, X. F. Wu, N. Han and Y. F. Chen, *Catal. Commun.*, 2018, **106**, 25–29.

198 J. Z. Ma, C. X. Wang and H. He, *Appl. Catal., B*, 2017, **201**, 503–510.

199 G. X. Zhu, J. G. Zhu, W. J. Jiang, Z. J. Zhang, J. Wang, Y. F. Zhu and Q. F. Zhang, *Appl. Catal., B*, 2017, **209**, 729–737.

200 W. X. Tang, H. D. Liu, X. F. Wu and Y. F. Chen, *Ozone: Sci. Eng.*, 2014, **36**, 502–512.

201 D. Mehandjiev, A. Naydenov and G. Ivanov, *Appl. Catal., A*, 2001, **206**, 13–18.

202 H. Fan, C. F. Zhao, Z. S. Ma and Y. K. Yang, *Environ. Pollut.*, 2020, **267**, 115164.

203 G. X. Zhu, W. Zhu, Y. Lou, J. Ma, W. Q. Yao, R. L. Zong and Y. F. Zhu, *Nat. Commun.*, 2021, **12**, 4152.

204 Y. Liu and P. Y. Zhang, *J. Phys. Chem. C*, 2017, **121**, 23488–23497.